scientific reports

Check for updates

OPEN

AI-driven adaptive vibration control in smart plate systems: a sustainable approach for next-generation sports engineering

Bing Lin[1], Jinyu Wang[1], Mehran Safarpour[2]✉ & Murat Yaylacı[3,4]

The current paper proposes an AI-based method for the vibration control of smart plate systems. The application is set for next-generation sports engineering, where performance enhancement is the main goal. The system consists of a core of coarse aggregate ultra-high-performance concrete (CA-UHPA) and piezoelectric face sheets, which are mounted on an elastic foundation. The properties of the material composite are foreseen based on the Halpin–Tsai models and the law of mixtures. Looking into the system's dynamic performance in a very thorough way is done using the quasi-3D theory having four variables. This theory gives the opportunity for the full consideration of the distribution of transverse shear strains and stresses throughout the plate thickness. The governing equations of the resonant response are derived by employing the concept of piezoelectricity together with Hamilton's energy principles. The elastic foundation is analyzed using both Winkler and Pasternak coefficients, thereby allowing the interaction of the plate and its support substrate to be included. The solution is achieved through using the physics-informed neural networks (PINNs) technique, which not only accurately and efficiently replaces the conventional Legendre Polynomial Expansions with deep neural networks (DNNs) for more computational efficiency and accuracy but also doubles the legacy of AI-powered methods in terms of real-time system adaptability and optimal vibration control under changing scenarios. A DNN-based verification process assists in obtaining and confirming the trustworthiness of the results. This research marks above all and the first time as a very promising new direction in the smart systems vibration control area in sports, and it is highly anticipated that the new development will have a positive impact on the performance and durability optimization of advanced sports equipment. The introduced method embodies a patent-driven technology leap in vibration control, where AI and new materials join forces to solve challenging problems.

Keywords AI-driven vibration control, Coarse aggregate ultra-high-performance concrete, Piezoelectric materials, PINNs, Smart plate systems

Nanocomposite structures are of great importance to engineers as they synergize the specific characteristics of nanomaterials and the flexibility of conventional materials, which in turn leads to better mechanical, electrical, and thermal performance[1]. These materials can be modified to possess excellent strength and longevity while being light in weight at the same time, which is a great advantage in sectors such as aerospace, automotive, and construction[2,3]. The introduction of nanoparticles in the matrix gives one the opportunity to have more control over the characteristics of the material, which includes, among others, better resistance to wear, corrosion, and environmental degradation[4]. Besides, the field of nanocomposites includes the notable aspect of energy efficiency with a very wide range of applications, such as lightweight structures and energy storage systems[5,6]. Their peculiar properties make it possible to produce high-performance coatings, sensors, and advanced composites for various applications[7,8]. The ability to customize the properties of nanocomposites at the molecular level brings forth a major breakthrough in the field of smart, responsive materials[9,10]. For engineers, comprehending and utilizing these materials is the key to stimulating innovation and enhancing the capacity and sustainability of contemporary technological advances.

[1]Chongqing Preschool Education College, Chongqing 404047, China. [2]Department of Mechanical Engineering, Faculty of Engineering, Tarbiat Modares University, Tehran, Iran. [3]Department of Civil Engineering, Recep Tayyip Erdogan University, 53100 Rize, Turkey. [4]Turgut Kıran Maritime Faculty, Recep Tayyip Erdogan University, 53900 Rize, Turkey. ✉email: m_safarpour@modares.ac.ir; safarpour74@gmail.com

One of the most important things to consider in engineering design is stability analysis, because it prevents structures and systems from being damaged by loads and environmental conditions, thus saving the clients' computational cost[11,12]. Moreover, it allows the engineers to predict and evaluate the response of a structure when different forces are applied, whether static, dynamic, or thermal[13]. In other words, an unstably analyzed structure could be the reason for a collapse or rupture and thus lead to expensive repairs or even disastrous errors[14,15]. To put it in another way, stability analysis is absolutely necessary for safety in the case of structures, like bridges, buildings, or dams, whose failure might cause the loss of lives or considerable property damage[16,17]. Taking into account the limits of material strength and structural design, the engineers can come up with better designs that do not allow for buckling, instability, or collapse[18,19]. Stability analysis in dynamic systems helps the engineer to find out whether vibrations, resonances, or oscillations will negatively impact or otherwise affect the performance and life span of a system[20,21]. In addition, stability analysis is imperative when it comes to designing efficient transportation systems such as highways, railways, and aircraft, where instability, no matter how small, can lead to serious accidents[22,23]. Not only that, but analysis is needed while designing energy systems, too, such as wind turbines or power grids, where maintaining stability at fluctuating loads is a must for uninterrupted operation[24,25]. In civil engineering, stability analysis aids the foundations of a building by assuring that they can bear its weight without causing the structure to tip or sink[26,27]. It is necessary to analyze stability because it tells when reinforcements need to be added, like bracing or supports, for the purpose of the structure's overall resistance[28]. But apart from this, stability analysis is also a must in the exact conditions of mechanical systems, thus making the components not be disabled by excessive pressure or vibration[29]. Besides this, for scientists involved in the material analysis area, stability analysis is a source of explanation about the behavior of composite materials when they are stressed, so they can choose the right materials for certain applications[30]. It is through this that engineers can spot weak parts in the design and rectify them early, which results in saving them time and computational cost[31]. If stability analysis is used in the design phase, then engineers can already get the structures to be efficient, safe, and durable, thus long-lasting performance with little maintenance[31]. Moreover, this is a particularly vital process in industries where the environmental and operational conditions are constantly changing like offshore engineering or aerospace[32]. In addition, analysis of the stability is one of the factors that contribute to the cost and safety in the design field, in which case the designs are optimized to satisfy both needs of functionality and finance[33]. Reliability in the design performance even under extreme circumstances or unpredictable situations is the main advantage of stability analysis[31].

Machine learning algorithms are the mainstay of the engineers' toolkit as they remove human involvement from data analysis and consequently help to detect the data patterns and make the predictions that otherwise would be very hard or very slow to obtain with traditional techniques[34,35]. Besides that, the algorithms can make the design processes faster and less prone to errors by providing accuracy in predictive maintenance, quality control, and resource allocation among other areas[36,37]. By making use of vast data collections, engineers can invent more intelligent systems that are able to adjust to the varying conditions, thus creating the fields of automation, robotics, and AI[38,39]. Machine learning can also provide the decisions to be made instantly, which is very important in fast-paced places like production, transport, and power generation systems[40]. In the end, the algorithms turn out to be the facilitators for engineers to work on intricate problems, to get better, and to spend less in a number of industries[41,42].

The smart plate system in sports engineering, particularly in tennis rackets, is depicted in Fig. 1. The assessment of tennis rackets sporting equipment having the vibration control feature proves to be advantageous

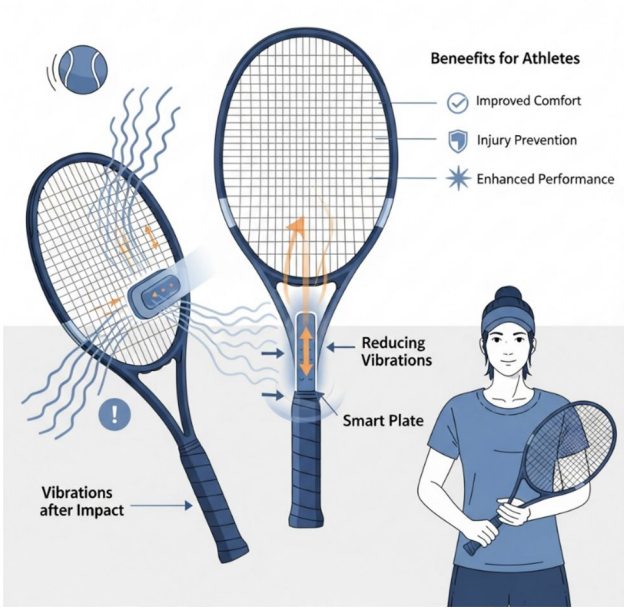

Fig. 1. Application of the smart plate system in sports engineering, particularly in a tennis racket.

for the players. Most of the time, the smart plate with the vibration-damping feature is presented as the solution to one of the problems in sports, i.e., the impact of the tennis ball. Moreover, the annoying vibrations surrounding the ball and their transmission to the player's hand lead to the experience of discomfort, fatigue, and in extreme cases, injury. The system, equipped with adaptive vibration control, can very much reduce these vibrations, permitting athletes to increase their comfort and also diminish the risk of injury. The combination of technology and real-time adaptive vibration control is such that it will transform the performance of the present-day athletes through material innovations. The smart plate not only incorporates the capacity factor to prolong the service life of sports equipment and to improve its performance, but also positively impacts the health of players, as one of the reasons for injuries is the reduced impact of vibrations. Thus, the system represents a big step forward in the industry; it will be the next generation of sports equipment that not only has practical advantages but also maximizes the performance of the athletes.

A conducted study for improvement in sports engineering has presented a novel AI-based adaptive vibration controlling system for the smart plate consisting of a coarse aggregate ultra-high-performance concrete core with piezoelectric face sheets and an elastic foundation. The properties of the composite system have been computed using Halpin–Tsai models and the law of mixtures. A sophisticated four-variable quasi-3D theory has been applied that captures the redistribution of transverse shear strains and stresses throughout the plate thickness, enhancing the predictions of dynamic response in the fabric. The theory of piezoelasticity and the principle of Hamilton have been deployed for drawing the governing equations concerning vibration behavior under load variations. The interaction of the elastic foundation with the plate has been modeled by considering both Winkler and Pasternak coefficients, thus dealing with the intricacies of structural support. The solution procedure has become significantly more efficient through the employment of PINNs, where deep neural networks perform other tasks, such as traditional Legendre Polynomial Expansions, to reach the governing equations quickly. This strategy makes it possible for real-time adaptive control letting vibration suppression to change with the altering system dynamics. The proposed model integrates two validated subsystems: piezo-elastic sandwich plates and foundation-structure interaction. The subsequent verification study first benchmarks these core components independently against established literature before presenting new results for the novel integrated system. The proposed method's reliability is further ratified through a DNN-based verification technique, confirming the strength and precision of the results. This work provides an eco-friendly and state-of-the-art solution for the vibration control of smart sports engineering systems. The AI-centered platform developed during this research shows a bright future in the optimization and durability enhancement of next-generation sports equipment, thus artfully combining advanced material systems and smart control strategies, redefining their very limits. This research has outlined the following major aspects: 1. The incorporation of AI-driven adaptive vibration control in real-time significantly improves the effectiveness of smart sports systems made of composite materials. 2. The vibration protection technology in various environments has been further developed through the combination of a CA-UHPA core and piezoelectric face sheets. 3. The four-variable quasi-3D theory considers the transverse shear strains and the stresses that are present throughout the thickness of the plate. 4. The combination of PINNs and DNNs leads to rapid but precise solutions for complex vibration control challenges.

Theory and formulation

Figure 2 presents the schematic of a sandwich smart plate assembly for adaptive vibration control. Many different layers with different mechanical properties constitute the system. The coarse aggregate ultra-high-performance concrete is the main structure where the central layer is surrounded by actuator and sensor layers at the top and bottom. Passing through these layers is a Pasternak elastic foundation that interacts with the ground layer, which is represented by the green section. In the coordinate system, the x_1, x_2, and x_3 axes specify the spatial dimensions of the plate and, where x_1 and x_2 are horizontal and x_3 is the thickness direction. The dimensions a

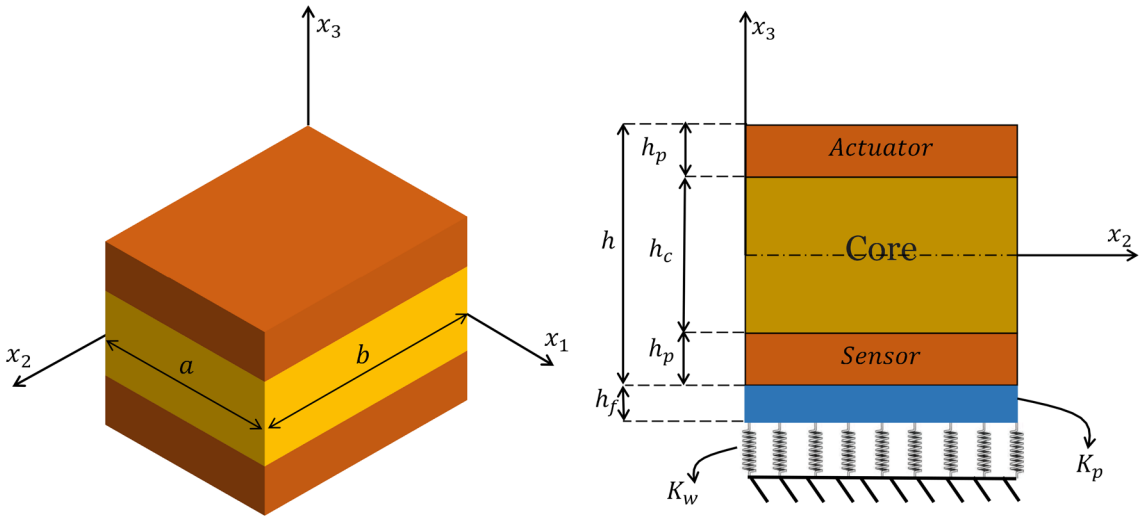

Fig. 2. The schematic of a sandwich smart plate assembly for adaptive vibration control.

and b indicate the length and width of the plate, whereas h_c, and h_p denote the total thickness of the system, the thickness of the actuator and sensor layers, and the thickness of the CA-UHPC core, respectively. The Winkler-Pasternak Foundation is represented by a spring constant K_w, and K_p, symbolizing the interaction between the plate and the elastic substrate. This setup enables the dynamic modeling of the vibrational behavior of the plate, as the actuators and sensors provide feedback control for the reduction of vibrations. The schematic is the starting point for the mathematical formulation that will be applied in the vibration control analysis, merging piezoelectric materials and the elastic foundation for better system performance.

There are two approaches to apply the CA (reinforcement distribution): uniformly (FG-UD) or functionally graded with two different patterns (FG-X and FG-O). Figure 3 shows these sorts of distributions.

Properties of composite media

The composite materials utilized in the disclosed system have remarkable characteristics that enhance their performance in the application of vibration control. The coarse aggregate ultrahigh-performance concrete bulk imparts enormous strength and durability, whereas the piezoelectric plates allow high energy conversion, thus giving an actuator and sensor with very quick response times. The pairing of these materials with an elastic foundation, which is illustrated with Winkler and Pasternak coefficients, boosts the system's dynamic property by taking substrate interactions into consideration. The Halpin–Tsai models and the law of mixtures employed provide the composite's mechanical properties' accurate prediction, hence bringing about better vibration damping and real-time adaptability.

Volume fraction of coarse aggregate (CA)

Through the plate thickness (x_3), the volume fraction of coarse aggregate (V_{CA}) may exhibit uniform (UD) or functionally graded (FG) distributions:

$$V_{CA}\left(\mathcal{X}_3\right)=\begin{cases} V_{CA}^{*} & FG-UD \\ 2\left(1-\frac{2|x_3|}{h}\right)V_{CA}^{*} & FG-O \\ 4\left(\frac{|x_3|}{h}\right)V_{CA}^{*} & FG-X \end{cases}, \tag{1}$$

where the highest volume percentage of CA is represented by V_{CA}^{*}. Equation (2) is used to produce V_{CA}^{*}.

$$V_{CA}^{*}=\frac{W_{CA}}{W_{CA}+\left(\frac{\rho^{CA}}{\rho^{m}}\right)-\left(\frac{\rho^{CA}}{\rho^{m}}\right)W_{CA}}, \tag{2}$$

where W_{CA} shows CNT mass fraction and ρ^{m}, ρ^{CA} are matrix and CA densities, respectively.

CA-UHPC's effective material qualities

The Halpin–Tsai models and the law of mixtures, adjusted for UHPC, are used to calculate the composite properties:

$$\begin{aligned} E_{11}&=\eta_1 V_{CA}E_{11}^{CA}+V_m E^m, \\ \frac{\eta_2}{E_{22}}&=\frac{V_{CA}}{E_{22}^{CA}}+\frac{V_m}{E^m}, \\ \frac{\eta_3}{G_{12}}&=\frac{V_{CA}}{G_{12}^{CA}}+\frac{V_m}{G^m}, \quad G_{12}^{CA}=E_{11}^{CA}\big/2\left(1+\nu_{CA}\right), \quad G^m=E^m/2\left(1+\nu_m\right) \\ \nu_{12}&=\nu_{CA}V_{CA}+\nu_m V_m \\ \nu_{21}&=\frac{\nu_{12}E_{22}}{E_{11}}, \\ \rho&=\rho_{CA}V_{CA}+\rho_m V_m \\ E_{33}&=E_{22}, \quad G_{12}=G_{13}=G_{23}, \quad \nu_{13}=\nu_{12}, \quad \nu_{31}=\nu_{21}, \quad \nu_{32}=\nu_{23}=\nu_{21} \end{aligned} \tag{3}$$

The effective elastic moduli are represented by E_{11} and E_{22}, the shear modulus by G_{12}, Poisson's ratios by ν_{12} and ν_{21}, and mass density by ρ. The formula $V_m=1-V_{CA}$ will be used to calculate the matrix's volume fraction. Moreover, size effects and the contribution of load applied to nanotubes and polymeric phases are

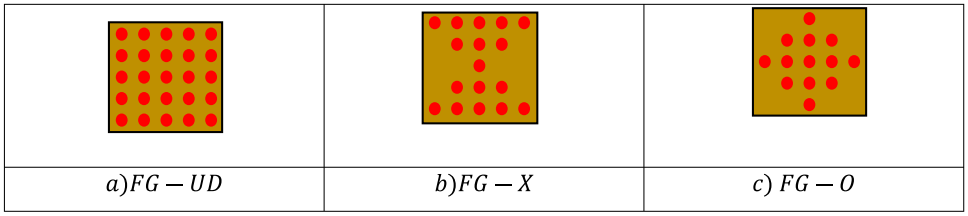

Fig. 3. Coarse aggregate distribution patterns in the plate's thickness.

connected to the efficiency metric $\eta_j (j = 1,2,3)$. The CA-UHPC core's material characteristics are presented in Table 1.

Mathematical model derivation

The displacement terms at a specific location across the plate thickness may be represented as follows in accordance with the four-variable quasi-3D theory[43].

$$u(x_1, x_2, x_3, t) = u_0(x_1, x_2, t) - x_3 w^b_{0,x}(x_1, x_2, t) + f(x_3) w^s_{0,x}(x_1, x_2, t), \tag{4a}$$

$$v(x_1, x_2, x_3, t) = v_0(x_1, x_2, t) - x_3 w^b_{0,y}(x_1, x_2, t) + f(x_3) w^s_{0,y}(x_1, x_2, t), \tag{4b}$$

$$w(x_1, x_2, x_3, t) = w^b_0(x_1, x_2, t) + g(x_3) w^s_0(x_1, x_2, t). \tag{4c}$$

where the four unknown variables are $w^{\mathrm{b}}_0, w^{\mathrm{s}}_0, u_0$, and v_0. where u_0 and v_0 represent the membrane displacements at the neural plane of the plate, i.e., $x_3 = 0$, in the x_1 and x_2 directions, respectively; w^b_0 and w^s_0 represent the vertical displacement at $x_3 = 0$ due to the bending and shear effects, respectively; t represents time; $f(x_3)$ and $g(x_3)$ represent the distribution of transverse shear strains and stresses across the thickness of the plate and are given as

$$f(x_3) = \frac{\pi}{h} x_3 - \frac{9\pi}{5h^3} x_3^3 + \frac{28\pi}{25h^5} x_3^5, \tag{5a}$$

$$g(x_3) = \frac{1}{8} f_{,x_3}(x_3). \tag{5b}$$

To put it simply, if we set $g(x_3) = 0$ in the equation above, then $\varepsilon_{x_3 x_3} = 0$. After assuming the linear small-deflection theory, the stresses are calculated as

$$\varepsilon = \{ \varepsilon_{x_1 x_1} \quad \varepsilon_{x_2 x_2} \quad \gamma_{x_1 x_2} \}^{\mathrm{T}} = \{ u_{,x_1} \quad v_{,x_2} \quad u_{,x_2} + v_{,x_1} \}^{\mathrm{T}} = \varepsilon_0 + x_3 \kappa_1 + f(x_3) \kappa_2, \tag{6a}$$

$$\gamma = \{ \gamma_{x_1 x_3} \quad \gamma_{x_2 x_3} \}^{\mathrm{T}} = \{ u_{,x_3} + w_{,x_1} \quad v_{,x_3} + w_{,x_2} \}^{\mathrm{T}} = [f_{,x_3}(x_3) + g(x_3)] \kappa_3, \tag{6b}$$

$$\varepsilon_{x_3 x_3} = w_{,x_3} = g_{,x_3}(x_3) w^s_0, \tag{6c}$$

with

$$\varepsilon_0 = \{ u_{0,x_1} \quad v_{0,x_2} \quad u_{0,x_2} + v_{0,x_1} \}^{\mathrm{T}}, \quad \kappa_1 = \{ -w_{0,x_1 x_1} \quad -w_{0,x_2 x_2} \quad -2w_{0,x_1 x_2} \}^{\mathrm{T}}, \tag{7a}$$

$$\kappa_2 = \{ w^s_{0,x_1 x_1} \quad w^s_{0,x_2 x_2} \quad w^s_{0,x_1 x_2} + w^s_{0,x_2 x_1} \}^{\mathrm{T}}, \quad \kappa_3 = \{ w^s_{0,x_1} \quad w^s_{0,x_2} \}^{\mathrm{T}}. \tag{7b}$$

Constitutive relations

Constitutive relations of the core layer

As per Hooke's rule, which is compatible with the restriction of σ^c_{33} being zero, the stress vector for the core layer may be expressed as follows: $\sigma^c = [\sigma^c_{x_1 x_1}, \sigma^c_{x_2 x_2}, \sigma^c_{x_3 x_3}, \sigma^c_{x_1 x_2}, \sigma^c_{x_1 x_3}, \sigma^c_{x_2 x_3}]^{TT}$. The following relationship connects the strain vector and stress tensor, $\boldsymbol{\varepsilon} = [\varepsilon_{x_1 x_1}, \varepsilon_{x_2 x_2}, \varepsilon_{x_3 x_3}, \gamma_{x_1 x_2}, \gamma_{x_1 x_3}, \gamma_{x_2 x_3}]^T$:

$$\boldsymbol{\sigma}^c = \mathbf{C}^c \boldsymbol{\varepsilon}, \tag{8}$$

The core layer's elastic constant matrix is denoted by $\mathbf{C}^c$.

Property	Coarse aggregate (CA)	UHPC matrix
Elastic modulus E_{11} (GPa)	70	45
Elastic modulus E_{22} (GPa)	70	45
Shear modulus G_{12} (GPa)	30	18
Poisson's ratio ν_{12}	0.15	0.20
Density ρ (kg/m^3)	2600	2400

Table 1. The CA-UHPC core's material characteristics.

$$
\begin{aligned}
\mathbf{C}^c &= \begin{bmatrix} \overline{Q}^c_{11} & \overline{Q}^c_{12} & \overline{Q}^c_{13} & 0 & 0 & 0 \\ \overline{Q}^c_{12} & \overline{Q}^c_{22} & \overline{Q}^c_{23} & 0 & 0 & 0 \\ \overline{Q}^c_{13} & \overline{Q}^c_{23} & \overline{Q}^c_{33} & 0 & 0 & 0 \\ 0 & 0 & 0 & \overline{Q}^c_{66} & 0 & 0 \\ 0 & 0 & 0 & 0 & \overline{Q}^c_{44} & 0 \\ 0 & 0 & 0 & 0 & 0 & \overline{Q}^c_{55} \end{bmatrix}, \\
\overline{Q}^c_{11} &= \frac{E_{11}}{\Delta}\left(1-\nu_{23}\nu_{32}\right), \quad \overline{Q}^c_{22} = \frac{E_{22}}{\Delta}\left(1-\nu_{31}\nu_{13}\right), \quad \overline{Q}^c_{33} = \frac{E_{33}}{\Delta}\left(1-\nu_{12}\nu_{21}\right), \\
\overline{Q}^c_{44} &= G_{23}, \quad \overline{Q}^c_{55} = G_{13}, \quad \overline{Q}^c_{66} = G_{12}, \quad \overline{Q}^c_{12} = \frac{E_{11}}{\Delta}\left(\nu_{21}+\nu_{31}\nu_{23}\right), \\
\overline{Q}^c_{13} &= \frac{E_{11}}{\Delta}\left(\nu_{31}+\nu_{21}\nu_{32}\right), \quad \overline{Q}^c_{23} = \frac{E_{22}}{\Delta}\left(\nu_{32}+\nu_{12}\nu_{31}\right), \\
\Delta &= 1-\nu_{12}\nu_{21}-\nu_{23}\nu_{32}-\nu_{31}\nu_{13}-2\nu_{12}\nu_{32}\nu_{13}.
\end{aligned} \tag{9}
$$

The top and bottom piezoelectric layers' constitutive relationships

The constitutive relationship of piezoelectric layers may be stated as follows using the theory of piezoelasticity:

$$
\begin{Bmatrix} \boldsymbol{\sigma^p} \\ D \end{Bmatrix} = \begin{bmatrix} \mathbf{C^p} & -\mathbf{e}^T \\ \mathbf{e} & \mathbf{A} \end{bmatrix} \begin{Bmatrix} \varepsilon \\ E \end{Bmatrix}. \tag{10}
$$

They have the following definitions because in Eq. (10), $\mathbf{C^p}$ stands for the elastic constant matrix for the piezoelectric layers, $\mathbf{E}$ for the dielectric permittivity constant matrix, and $\mathbf{e}$ for the electromechanical coupling matrix.

$$
\begin{aligned}
\mathbf{C^p} &= \begin{bmatrix} \overline{Q}^p_{11} & \overline{Q}^p_{12} & \overline{Q}^p_{13} & 0 & 0 & 0 \\ \overline{Q}^p_{12} & \overline{Q}^p_{22} & \overline{Q}^p_{23} & 0 & 0 & 0 \\ \overline{Q}^p_{13} & \overline{Q}^p_{23} & \overline{Q}^p_{33} & 0 & 0 & 0 \\ 0 & 0 & 0 & \overline{Q}^p_{66} & 0 & 0 \\ 0 & 0 & 0 & 0 & \overline{Q}^p_{44} & 0 \\ 0 & 0 & 0 & 0 & 0 & \overline{Q}^p_{55} \end{bmatrix}, \\
\mathbf{e} &= \begin{bmatrix} 0 & 0 & 0 & 0 & \overline{e}_{15} & 0 \\ 0 & 0 & \overline{e}_{15} & 0 & 0 & 0 \\ \overline{e}_{31} & \overline{e}_{31} & \overline{e}_{33} & 0 & 0 & 0 \end{bmatrix}, \\
\mathbf{A} &= \begin{bmatrix} \mathrm{A}_{11} & 0 & 0 \\ 0 & \mathrm{A}_{22} & 0 \\ 0 & 0 & \overline{\mathrm{A}}_{33} \end{bmatrix}.
\end{aligned} \tag{11}
$$

Piezoelectric material-related elastic matrix components are shown as

$$
\begin{aligned}
\overline{Q}^p_{1i} &= Q^p_{1i} - \frac{Q^p_{13}Q^p_{13}}{Q^p_{33}}, (i=1,2), \quad \overline{Q}^p_{66} = Q^p_{66}, \quad \overline{Q}^p_{44} = Q^p_{44}, \\
\overline{Q}^p_{j3} &= Q^p_{j3}, (j=1,2,3), \quad \overline{Q}^p_{31} = Q^p_{31} - \frac{Q^p_{13}e_{33}}{Q^p_{33}}, \\
\tilde{e}_{15} &= e_{15}, \quad \overline{\mathrm{A}}_{11} = \mathrm{A}_{11}, \quad \overline{\mathrm{A}}_{33} = \mathrm{A}_{33} + \frac{e^2_{33}}{Q^p_{33}}.
\end{aligned} \tag{12}
$$

Additionally, $\boldsymbol{\sigma^p}$, $\mathbf{E}$ and $\mathbf{D}$ represent the stress field in piezoelectric layers that satisfy the null $\sigma^p_{x_3x_3}$ condition, the electric field, and the electric displacement field, respectively. They may be written as follows:

$$
\begin{aligned}
\boldsymbol{\sigma}^{\mathrm{p}} &= \left[\sigma^p_{x_1x_1}, \sigma^p_{x_2x_2}, \sigma^p_{x_3x_3}, \sigma^p_{x_1x_2}, \sigma^p_{x_2x_3}, \sigma^p_{x_1x_3}\right]^{TT}, \\
\mathbf{D} &= \left[D_{x_1}, D_{x_2}, D_{x_3}\right]^{TT}, \\
\mathbf{E} &= \left[E_{x_1}, E_{x_2}, E_{x_3}\right]^{TT} = -\left[\Phi_{,x_1}, \Phi_{,x_2}, \Phi_{,x_3}\right]^{TT}.
\end{aligned} \tag{13}
$$

where Φ is the electrical potential function, which will subsequently be defined in accordance with the electrical boundary conditions. The assumption of linearity in the fluctuations of electric potential across their thickness is justified by the relatively thin piezoelectric layers. It is possible to represent the electrical potential function in the top and lower piezoelectric layers as follows:

$$
\Phi\left(x_1,x_2,x_3\right) = \begin{cases} -cos\left(\pi\left(\frac{2x_3-h_c-h_p}{2h_p}\right)\right)\psi_a(x_1,x_2) 0.5h_c < z < 0.5h_c + h_p \\ -cos\left(\pi\left(\frac{2x_3+h_c+h_p}{2h_p}\right)\right)\psi_s(x_1,x_2) - 0.5h_c - h_p < z < -0.5h_c \end{cases}, \tag{14}
$$

The electrical potential at the surfaces of the piezoelectric layers next to the core layer in the previously described connection is zero, since it is believed that these surfaces are grounded. Hamilton's principle, which is extended in the following way for the scenario being studied, is used to get the governing equations [44]:

$$\int_0^t (\delta U - (\delta T + \delta W_1 + \delta W_2 + \delta W_3))\mathrm{d}t = 0, \tag{15}$$

where t stands for any random moment in time. The following formula is used to calculate the sandwich plate's variations in strain energy (δU) and kinetic energy (δT):

$$\begin{aligned}
\delta U = & \int_0^b \int_0^a \int_{-0.5h_c}^{0.5h_c} \Big\{ \sigma^c_{x_1x_1}\delta\varepsilon_{x_1x_1} + \sigma^c_{x_2x_2}\delta\varepsilon_{x_2x_2} + \sigma^c_{x_3x_3}\delta\varepsilon_{x_3x_3} \\
& + \sigma^c_{x_1x_2}\delta\gamma_{x_1x_2} + \sigma^c_{x_2x_3}\delta\gamma_{x_2x_3} + \sigma^c_{x_1x_3}\delta\gamma_{x_1x_3} \Big\} \mathrm{d}x_3\mathrm{d}x_1\mathrm{d}x_2 \\
& + \int_0^b \int_0^a \int_{0.5h_c}^{0.5h_c+0.5h_p} \Big\{ \sigma^p_{x_1x_1}\delta\varepsilon_{x_1x_1} + \sigma^p_{x_2x_2}\delta\varepsilon_{x_2x_2} + \sigma^p_{x_3x_3}\delta\varepsilon_{x_3x_3} + \sigma^p_{x_1x_2}\delta\gamma_{x_1x_2} \\
& + \sigma^p_{x_2x_3}\delta\gamma_{x_2x_3} + \sigma^p_{x_1x_3}\delta\gamma_{x_1x_3} - D_{x_1}\delta E_{x_1} - D_{x_2}\delta E_{x_2} - D_{x_3}\delta E_{x_3} \Big\} \mathrm{d}x_3\mathrm{d}x_1\mathrm{d}x_2 \\
& + \int_0^b \int_0^a \int_{-0.5h_c-0.5h_p}^{-0.5h_c} \Big\{ \sigma^p_{x_1x_1}\delta\varepsilon_{x_1x_1} + \sigma^p_{x_2x_2}\delta\varepsilon_{x_2x_2} + \sigma^p_{x_3x_3}\delta\varepsilon_{x_3x_3} + \sigma^p_{x_1x_2}\delta\gamma_{x_1x_2} \\
& + \sigma^p_{x_2x_3}\delta\gamma_{x_2x_3} + \sigma^p_{x_1x_3}\delta\gamma_{x_1x_3} - D_{x_1}\delta E_{x_1} - D_{x_2}\delta E_{x_2} - D_{x_3}\delta E_{x_3} \Big\},
\end{aligned} \tag{16a}$$

$$\begin{aligned}
\delta T = & \int_0^b \int_0^a \int_{-0.5h_c}^{0.5h_c} \left\{ \rho^{(k)} \left\{ \dot{u}\delta\dot{u} + \dot{v}\delta\dot{v} + \dot{w}\delta\dot{w} \right\} \right\} \mathrm{d}x_3\mathrm{d}x_1\mathrm{d}x_2 \\
& + \int_0^b \int_0^a \int_{0.5h_c}^{0.5h_c+0.5h_p} \left\{ \rho^p \left\{ \dot{u}\delta\dot{u} + \dot{v}\delta\dot{v} + \dot{w}\delta\dot{w} \right\} \right\} \mathrm{d}x_3\mathrm{d}x_1\mathrm{d}x_2 \\
& + \int_0^b \int_0^a \int_{(-0.5h_c-0.5h_p)}^{(-0.5h_c)} \left\{ \rho^p \left\{ \dot{u}\delta\dot{u} + \dot{v}\delta\dot{v} + \dot{w}\delta\dot{w} \right\} \right\} \mathrm{d}x_3\mathrm{d}x_1\mathrm{d}x_2,
\end{aligned} \tag{16b}$$

Additionally, the elastic substrate's variation in work would be calculated as follows:

$$\delta W_1 = \int_A \left(-K_w w + K_p \nabla^2 w \right) \delta w dA. \tag{17}$$

The symbols K_w, and K_p stand for the foundation's Winkler coefficient and Pasternak coefficient, respectively. A transversely distributed external force's virtual work, $f(x_1, x_2, t)$, is computed using

$$\delta W_2 = \int_A (f\,(x_1, x_2, t)\,\delta w\,(x_1, x_2, t))dA. \tag{18}$$

The change in the work done with respect to the electric force that is applied externally:

$$\delta W_3 = \int_A \left(N^P \nabla^2 w \right) \delta w\,(x_1, x_2, t)\,dA. \tag{19}$$

The external electric load is represented by N^P. The following method may be used to calculate the electric load:

$$N^P = -2\left(e_{31} - \frac{c_{13}e_{33}}{c_{33}} \right) \phi_0. \tag{20}$$

ϕ_0 represents the initial external electric potential. Finally, the governing equations and boundary conditions may be obtained by replacing Eq. (15) with Eqs. (16), (17), (18), and (19).

PINNs solution procedure

Following a structured approach for physics-informed modeling of piezoelectric systems[45], the governing equations are embedded into a deep neural network training framework. PINNs, or physics-informed

neural networks, are considered a cutting-edge computational strategy for the numerical solution of physical phenomena' partial differential equations (PDEs). Neural networks are not only trained on data but also on the physics described by the equations, as traditional numerical methods do. The process of obtaining the solution is as follows: the governing equations, for instance, elasticity or fluid dynamics, are coded into the loss function of the neural network. Hence, the model learns from both data and the underlying physics represented by the equations. In the real-world application, PINNs take the residuals of the PDEs as part of the training process, thereby enforcing the physical constraints. This results in accurate and efficient solutions, particularly in complex problems where traditional methods may fail to be effective. The use of neural networks instead of classical polynomial expansions (e.g., Legendre polynomials) has made PINNs a powerful tool by providing substantial gain in computational efficiency and the capability of dealing with high-dimensional nonlinear systems. This approach is very beneficial in the area of adaptive vibration control systems as it provides near real-time solutions to the prediction of dynamic behaviors. It should be highlighted that the governing equations coded into the PINN loss function are the complete set derived in Sections "Mathematical model derivation" and "Constitutive relations", which inherently include both the piezo-elastic coupling and the foundation terms. The boundary conditions in the loss can represent various edge conditions in conjunction with the foundation.

Replace Legendre polynomial expansions with neural networks (NNs)

We use deep neural networks to estimate the displacement and electric potential fields rather than Legendre polynomial expansions (Eqs. 21a–21f):

$$u_0\left(x_1, x_2, t\right) = N_{u_0}\left(x_1, x_2, t, \theta\right), \tag{21a}$$

$$v_0\left(x_1, x_2, t\right) = N_{v_0}\left(x_1, x_2, t, \theta\right), \tag{21b}$$

$$w_0^b\left(x_1, x_2, t\right) = N_{w_0^b}\left(x_1, x_2, t, \theta\right), \tag{21c}$$

$$w_0^s\left(x_1, x_2, t\right) = N_{w_0^s}\left(x_1, x_2, t, \theta\right), \tag{21d}$$

$$\psi_a\left(x_1, x_2, t\right) = N_{\psi_a}\left(x_1, x_2, t, \theta\right), \tag{21e}$$

$$\psi_s\left(x_1, x_2, t\right) = N_{\psi_s}\left(x_1, x_2, t, \theta\right). \tag{21f}$$

where θ stands for the neural networks' trainable weights and biases. With inputs (x_1, x_2, t), each N is a deep neural network.

Initial and boundary conditions

The loss function is represented using boundary and beginning conditions:

- Clamped BCs:

$$L_{BC} = \sum \left|\left|u_0\left(\partial\Omega, t\right)\right|\right|^2 + \left|\left|\nabla u_0\left(\partial\Omega, t\right)\right|\right|^2 + \cdots. \tag{22}$$

- Initial Conditions:

$$L_{IC} = \sum \left\|u_0\left(x_1, x_2, 0\right) - u_0^{data}\right\|^2 + \left\|\dot{u}_0\left(x_1, x_2, 0\right) - \dot{u}_0^{data}\right\|^2 + \cdots. \tag{23}$$

Governing PDE residuals

The residuals of the electromechanical PDEs are enforced:

- The mechanical residual: $R_m = m\ddot{u} + C\dot{u} + Ku - f$
- Maxwell's Equations for Electrical Residual: $Re = \nabla \cdot D - q = 0$

Total lack of PDE: $L_{PDE} = \sum \|Rm\|^2 + \|\mathrm{Re}\|^2$

The sensor-actuator relationship and the PD controller

Soft constraints encode the sensor-actuator dynamics:

$L_{\psi_s} = \left\|\psi_s - \left[k_{\psi\psi}^{-1}\right]_s \left[k_{\psi u}\right]_s u_s\right\|^2$ is the sensor potential.

$L_{\psi_a} = \left\|\psi_a - \left(G_v\dot{\psi}_s - G_d\psi_s\right)\right\|^2$ is the actuator potential.

Changes to damping and stiffness

Adding adjusted stiffness and Rayleigh damping:

- Damping Term: $C = \alpha R_m + \beta R_k u + G_v[k_{\psi u}]_a[k_{\psi\psi}^{-1}]_s[k_{\psi u}]_s$
- Stiffness Term: $K = k_{uu} + G_d[k_{\psi u}]_a[k_{\psi\psi}^{-1}]_s[k_{\psi u}]_s$

Training loss function

The function of complete loss:

$$L_{total} = \lambda_{PDE} L_{PDE} + \lambda_{BC} L_{BC} + \lambda_{IC} L_{IC} + \lambda_{\psi_s} L_{\psi_s} + \lambda_{\psi_a} L_{\psi_a} + \lambda_{charge} L_{charge}. \tag{24}$$

where weighting hyperparameters are represented by λ terms.

Rayleigh damping coefficients

In order to minimize L_{total}, the coefficients α_R and β_R are were trained using gradient descent.

Steps in implementation

1. Describe the designs of neural networks for every field variable.
2. A sample of collocation points in the space (x_1, x_2, t).
3. Use automated differentiation to calculate derivatives.
4. Create loss terms for control relations, BCs, ICs, and PDEs.
5. Use a gradient-based optimizer to train the NNs by minimizing L_{total}.

DNN-based verification procedure

DNN's methodology finds its application particularly in the validation and confirmation of results from complex engineering models, and it is most effective when dealing with systems characterized by complex dynamic behavior, such as adaptive vibration control. DNNs, which are referred to as deep neural networks, are nothing but multi-layered structures that can learn to recognize important features and also get the patterns from the data that is very large. In the current work, DNNs serve as the tools for comparing and verifying the outputs that the PINNs have produced. By training the neural network on known solution sets, DNNs can easily predict the system's response with different kinds of conditions set, and in doing so, they will be able to assert the correctness of the PINNs-based predictions. The DNN method is characterized by taking up the model for training by using a huge amount of simulation data, which leads to the ability of the model to find the solution to the problem of vibration control. DNN can also signal the presence of any inconsistencies or errors in the PINNs model by comparing predicted outcomes with certain benchmarked or experimental results that are already known. After the training is complete, the DNN becomes a powerful and, at the same time, computation-saving approach to the validation of the solutions, thereby confirming their dependability and, at the same time, upgrading the predictive power of the system. Also, DNNs contribute to the solution's robustness by taking into account both the data and the physical law that is incorporated in the PINNs framework, thus providing a smooth merger of AI and physical modeling. The approach mentioned above guarantees that the conclusions drawn will be correct as well as suitable for the application in smart systems that are associated with the real world.

The development of the DNN algorithm

The evolution of the DNN algorithm relies on the creation of multi-layered architectural structures that possess the capability to extract very detailed features from data. The algorithm first passes the raw input data through a chain of layers, where each layer is responsible for a certain transformation. These transformations are able to convey abstract qualities to the model that let the latter better capture the nonlinear mappings among inputs and outputs. The DNN training process consists of weight adjustments of the model through the backpropagation method and the use of gradient descent techniques for error minimization between the predicted results and the real outcomes. Step by step, the DNN algorithm becomes very good at imitating complex systems; thus, it can be used in areas such as noise control to derive predictions as well as validations that are very close to the real ones.

Forward propagation

The process of determining the output of the network based on the input is called forward propagation in DNN. It is done by taking the input layer-wise through the network, and each layer does a weighted summation of the inputs, followed by an activation function process. The forward propagation through one layer can be represented by the following general equation:

$$z^{(l)} = W^{(l)} * a^{(l-1)} + b^{(l)}. \tag{25}$$

where $z^{(l)}$, $W^{(l)}$, $a^{(l-1)}$, and $b^{(l)}$ are the vector of the weighted sum for the $l-th$ layer, the weight matrix for the $l-th$ layer, the activation vector from the previous layer (or input layer for the first layer), the bias vector for the $l-th$ layer. After computing the weighted sum, the activation function σ is applied:

$$a^{(l)} = \sigma\left(z^{(l)}\right). \tag{26}$$

where $a^{(l)}$ and $\sigma(\cdot)$ show the output of the l-th layer (or the activation for that layer), and the activation function, which introduces nonlinearity into the model. For the final output layer, the network produces the prediction:

$$y_{pred} = a^{(L)}. \tag{27}$$

In this case, L denotes the overall number of layers while y_{pred} indicates the value predicted by the network. For each input that goes through the network, the forward propagation process is carried out again, enabling the model to make predictions through the identification of features it has already learned.

Backpropagation and optimization

Backpropagation is a very sensitive illustration of the training method that was used by the model, functions of the neural net that are modified by the machine based on the loss function's gradients displayed for every weight. This way, the neural net can continuously learning through the reduction of the loss function, the output closer and closer to the prediction. The entire procedure consists of two main stages: one is applying the chain rule to derive the gradients, and the other is using an optimization technique, such as the most commonly used one, which is gradient descent, to perform the weight adjustments. The loss function is expressed mathematically as $L(y_{true}, y_{pred})$, where y_{true} denotes the actual class and y_{pred} represents the output of the network. The expression of the gradients for the loss function regarding the weights is obtained using the chain rule. For the output layer L, the gradient of the loss concerning the output is:

$$\partial L/\partial a^{(L)} = \nabla a^{(L)} L. \tag{28}$$

For hidden layers, the gradient is propagated backward through the network. For layer , the gradient of the loss with respect to the weighted sum $z^{(l)}$ is:

The gradient of the loss with respect to the weights at layer is:

$$\partial L/\partial W^{(l)} = \partial L/\partial z^{(l)} * \left(a^{(l-1)}\right)^T. \tag{29}$$

Once the gradients are calculated, the weights and biases are updated using an optimization algorithm, such as gradient descent. For gradient descent, the update rule is:

$$W^{(l)} \leftarrow W^{(l)} - \eta * \partial L/\partial W^{(l)}. \tag{30}$$

where η is the learning rate. The biases are updated similarly:

$$b^{(l)} \leftarrow b^{(l)} - \eta * \partial L/\partial b^{(l)}. \tag{31}$$

The backpropagation technique works by passing through these layers one after the other, starting from the output layer, which is the first layer, followed by the input layer, and simultaneously frequently changing the weights and bias to lower the loss function. Thus, the neural network can produce the output by fine-tuning the parameters in such a way that the error between the predicted and the actual output is minimized, consequently boosting its performance.

Verification workflow

The verification process that is based on the DNN, which is employed to verify the genuineness of the solutions of the physics-informed neural networks (PINN) for the smart plate system, involves four steps as depicted in Fig. 4. In the first step, high-fidelity displacement and voltage fields U_{PINN} are generated by the PINN solver. Then, a supervised DNN model is formed whose inputs are the spatio-temporal coordinates (x, t) and whose targets are the fields executed by the PINN, thus completing the second step. The DNN subsequently predicts

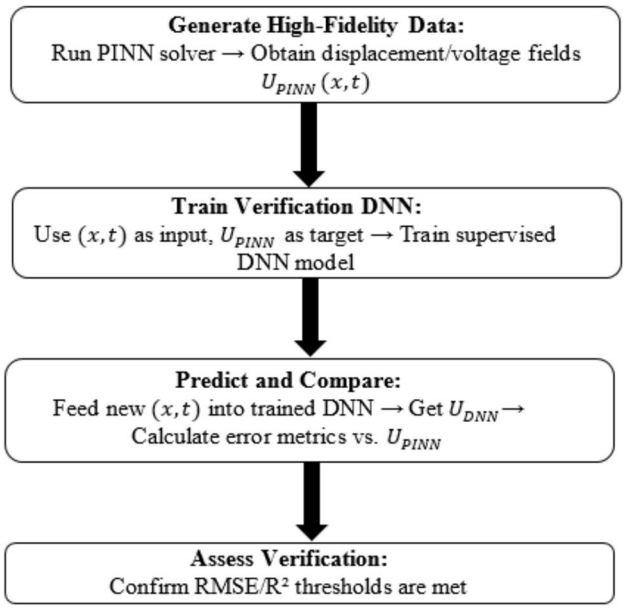

Fig. 4. The DNN-based verification process, which is used to determine the validity of the PINN solutions for the smart plate system.

the system response U_{DNN} for new input locations and calculates the error metrics (RMSE, R^2) with respect to the PINN reference as part of the third step. Ultimately, at the last step, the metrics are validated by whether or not they satisfy the predetermined thresholds, which, in turn, provide a check for the AI-driven methodology's reliability and consistency, thus guaranteeing the independent verification of the entire process.

Additionally, the dimensionless parameters may be written like this:

$$K_W^* = \frac{K_w a^4}{E_m I}, \quad K_P^* = \frac{K_p a^2}{E_m I}, \quad \Omega = \omega a \sqrt{\frac{\rho_m}{E_m}}, \quad \phi_0^* = \frac{\phi_0}{10^2\,(V)}, \quad W^* = w/h, \quad T^* = t/t_{\max}. \tag{32}$$

Results and discussion

Verification study

To verify the accuracy of the formulated piezo-elastic governing equations and the numerical solution procedure, the model is first applied to benchmark cases from the literature. Table 2 validates the implementation for functionally graded plates with integrated piezoelectric layers under various electrical boundary conditions[46]. Subsequently, Table 2 validates the modeling of the elastic foundation interaction for a functionally graded plate[47]. The excellent agreement in these component-level benchmarks establishes confidence in the framework's capability to handle the coupled physics of the CA-UHPC-based smart plate system on an elastic foundation, whose new results are presented in the following sections.

The first three natural frequencies of clamped-edge, square, functionally graded plates reinforced with graphene nanoplatelets (GPL) are compared in Table 2 under the different conditions of open and closed boundary with the outcomes of Ref.[46]. The comparison offers insight into the accuracy and consistency of the proposed model as it includes both the existing references and the present study's results. For the UD type, the natural frequencies under the closed and open conditions are virtually the same, with only slight discrepancies between the reference results and the present findings. To illustrate, in the closed condition, Ω_1 is 182.654 Hz in the reference and 182.641 Hz in the present study, indicating a difference that can be considered negligible. The consistency that appears in both the reference and present results indicates the reliability of the model that was used in the present study for uniform distribution. In the case of FG-X and FG-O types, the comparison shows similar trends, with the natural frequencies between the two conditions being very close. In the closed electrical condition, for example, the first natural frequency Ω_1 for the FG-X type is 184.103 Hz in the reference and 184.089 Hz in the present study. These minor differences confirm the precise nature of the present methodology for piezoelectric plate systems with functionally graded material properties. Moreover, the frequency shifts caused by the open and closed conditions illuminate the role of the electrical boundary constraints in the dynamic behavior of the system. In conclusion, the results of the present study are in very good agreement with the reference values, thus asserting the power of the proposed model in the analysis of the natural frequencies of piezoelectric reinforced plates.

Table 3 illustrates the non-dimensional natural frequency comparison for various-sized plates of FG material, that are resting on different kinds of Winkler foundations, and the shear modulus varying with reference to the power-law index. The non-dimensional frequencies $\overline{K}_w = \frac{K_w b^4}{D_m}$ and $\overline{K}_p = \frac{K_p b^2}{D_m}$ were used for their calculation, where b is the side length of the plate and D_m is the bending power of the plate. Frequencies being compared for the present study and Ref. [47] mean to evaluate the accuracy and consistency of the proposed model. In the case of n = 0, the most stable material distribution that exists, the natural frequencies of the present study coincide with those of Ref.[47] but with slight differences. For instance, at $\overline{K}_w$=0 and $\overline{K}_p$ = 0, the corresponding natural frequency is 0.0290 in the present study and 0.0291 in Ref.[47], allowing for a conclusion of a very minor difference. The same close match is found for the case with $\overline{K}_w$ = 100 and $\overline{K}_p$ = 0, where the frequency in the current study is 0.0296 while in the reference it is 0.0298. Even at $n = 0$, highlighting the use of a functionally graded material with continuously varying properties, the differences in the natural frequencies were still very

Type	Condition	Reference	Ω_1	Ω_2	Ω_3
UD	Closed	Ref. [46]	182.654	444.452	444.452
		Present	182.641	444.441	444.441
	Open	Ref. [46]	198.763	480.824	480.824
		Present	198.751	480.813	480.813
FG-X	Closed	Ref. [46]	184.103	447.831	447.831
		Present	184.089	447.820	447.820
	Open	Ref. [46]	200.080	483.861	483.861
		Present	200.069	483.850	483.850
FG-O	Closed	Ref. [46]	181.191	441.040	441.040
		Present	181.180	441.029	441.029
	Open	Ref. [46]	197.437	477.761	477.761
		Present	197.426	477.752	477.752

Table 2. The first three natural frequencies for clamped-edge, square, GPL reinforced plates with integrated piezoelectric layers ($W_{GPL} = 0.1\,[wt\%]$, $a = b = 1\,[m]$, and $h_p = 0.025$).

$\overline{K}_w$	$\overline{K}_p$	$n=0$		$n=1$	
		Ref.[47]	Present	Ref.[47]	Present
0	0	0.0291	0.0290	0.0227	0.0225
	100	0.0406	0.0404	0.0382	0.0380
100	0	0.0298	0.0296	0.0238	0.0236
	100	0.0411	0.0408	0.0388	0.0386

Table 3. The FG square plate's non-dimensional natural frequency, $\varpi = \omega h\sqrt{\frac{\rho_m}{E_m}}$, with relation to the power law index, shear, and Winkler parameters ($\overline{K}_w = \frac{K_w b^4}{D_m}$, $\overline{K}_p = \frac{K_p b^2}{D_m}$)

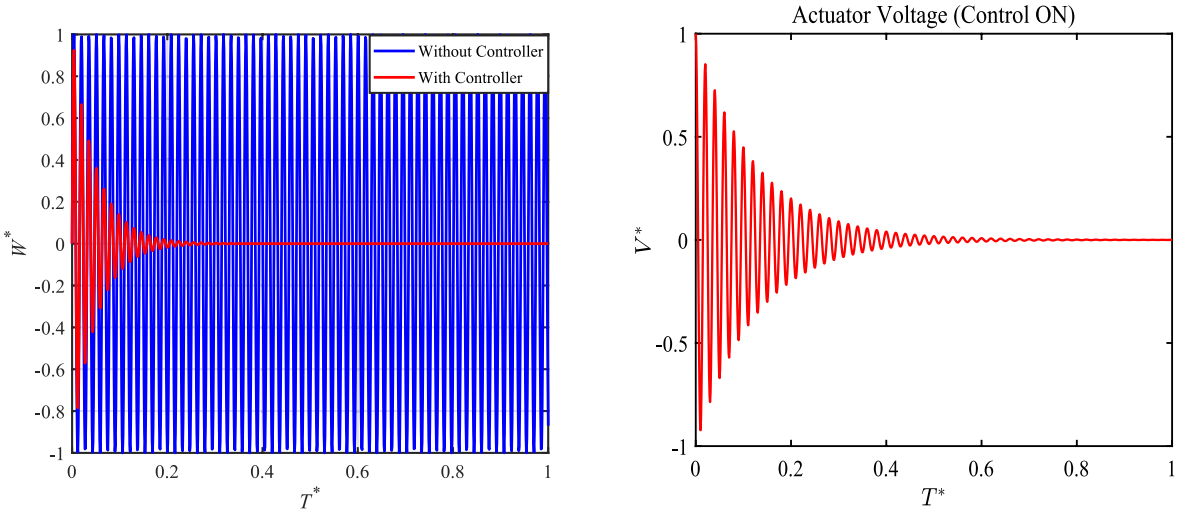

Fig. 5. The vibration response and dimensionless actuator voltage of the smart plate system, illustrating the effects of an adaptive vibration controller.

small. For example, with $\overline{K}_w = 0$ and $\overline{K}_p$=0, the present study gives 0.0225, and Ref.[47] gives 0.0227 as the values. With $\overline{K}_w = 100$ and $\overline{K}_p = 0$, the present study gives 0.0236 as the frequency, which is slightly lower than the reference value of 0.0238. In general, the table illustrates that the present study's natural frequency predictions are in perfect agreement with the reference values, thus confirming the validity of the method proposed for the dynamic analysis of functionally graded plates with Winkler and shear foundation parameters. The minor differences noticed might be due to variations in the numerical model, but they do not affect the overall reliability of the technique.

Parametric results

The proposed adaptive vibration controller is shown to be effective for the smart composite plate system through a rigorous performance test depicted in Fig. 5. At the core of the illustration is the vibrational response of the system without any dimensionless quality adjustment against two main operational states and the dimensionless time. The blue curve marked "Without Controller" shows a considerable vibrating amplitude that takes a long time to die down, which is a typical behavior of an underdamped system that is still vibrating. On the other hand, the red curve ("With Controller") is a sign of the controller's success, as there is a huge decrease in the peak amplitude and a quick settling down to the equilibrium point. This visual comparison provides quantitative proof of the hypothesis that the controller has played a key part in increasing damping and simultaneously suppressing vibrations actively. Also, the figure shows the time history of the corresponding dimensionless actuator voltage that was needed to produce the "With Controller" response. This information, which is drawn, is essential for judging the practical feasibility of this case. It shows that the control signal needed for the vibration reduction presented stays within the operational limits for commonly used piezoelectric materials, and accordingly, no issues of physical realizability are raised. The two datasets in this figure present a clear overall demonstration: the upper plot shows the control objective (the reduction of the vibration), and the lower plot gives evidence of the method's practicality by portraying the control input that can be achieved, the AI-driven adaptive control strategy is made more viable.

To assess the physical realizability of the control action, the generated actuator voltage profile for the case in Fig. 5 is presented. For the specific piezoelectric material properties considered (e.g., PZT-5A), the peak dimensionless voltage of 1 corresponds to a maximum electric field. This value is substantially lower than the typical coercive field (~500 to 1000 V/mm) and breakdown strength (~1000 to 2000 V/mm) for such materials[48]. Therefore, the proposed adaptive control scheme operates within safe, non-depolarizing electrical limits.

The adaptive controller is implemented as a PD feedback loop, as formulated in Section "The sensor-actuator relationship and the PD controller". Figure 6 illustrates the system response for two distinct sets of controller gains. This figure shows how different control variables' changes positively or negatively affect the system's vibration response. The plot compares two sets of parameters related to the proportional-derivative controller and presents the dimensionless deflection versus dimensionless time. The first set of parameters produces a slower damping process in the system, observed by a slight decrease in deflection, and the second set of parameters, however, leads to a quicker decay of the vibration. Thus, it seems that larger controller parameters make the system less responsive to vibrations, and, moreover, they not only speed up the decay but also result in faster stabilization. The dynamic behavior of the system, which is controlled through the power of these control parameters, is the one that gets optimized for smart systems. The vibratory response would then be tuned as per the variations in the parameters, which means if the conditions of the system change, so will its adaptability, hence leading to the control being overall more efficient and less time-consuming. Along with that, it also indicates how significant a factor precise tuning is in modern smart systems since their real-time adaptability is one of the major prerequisites in sports or high-performance tech-related applications. Real-time control of these parameters produces maximum vibration suppression and performance enhancement under different conditions.

Figure 7 illustrates the dependence of the dimensionless voltage applied on the system's frequency for various height-to-width ratios. The height-to-width ratio specifies the size relations of the plate dimensions, and it is a crucial parameter that brings about the system's behavior under voltage application. The curves indicate that the higher the applied voltage, the lower the frequency of the system, which is clearly seen in the downward slope of the curves. Furthermore, the plot presents the height-to-width ratios, each curve depicting a certain ratio. As the frequency decreases, the ratio increases, thus the system's vibration is largely determined by the plate's geometry. The lowest ratio is depicted by the blue line, while, in order, the red, green, and purple lines illustrate increasingly larger ratios. The impact of the height-to-width ratio on the frequency is essential for the design of smart plate systems. It is possible to control the vibrational characteristics by changing the height-to-width ratios. For instance, in sports engineering, where performance enhancement is a major concern, voltage and geometry interaction is a key factor in the design of more efficient systems that not only eliminate unwanted vibrations but also enhance the durability and comfort of the equipment.

Figure 8 depicts how the non-dimensional Winkler coefficient, which is the indicator of the plate's affinity with the base, is related to the frequency of the system. Different voltage levels are taken into account, while the graph shows the comparison of the Winkler coefficient's variations and the frequency of the system. The plot indicates that the system's frequency gets to shrink mostly when the Winkler coefficient reaches its maximum level, and this is quite visible from the curves that exhibit a downward trend. The minimum values of the Winkler coefficient corresponding to each voltage-applied condition are marked with red circles, which point out the places where the system's frequency is the lowest. These places point out the best setup for the reduction of vibrations in accordance with the specific voltage inputs. The effect of the applied voltage on the dynamic behavior of the system is quite clear; at lower values of the Winkler coefficient, the higher voltages result in a more pronounced decrease in frequency. This study is critical for the design of systems with the best possible vibration control, and among the factors affecting that, foundation stiffness is the most important one. In sophisticated smart systems, like those in athletics, varying the Winkler coefficient provides a very accurate tuning for both performance and vibration control purposes.

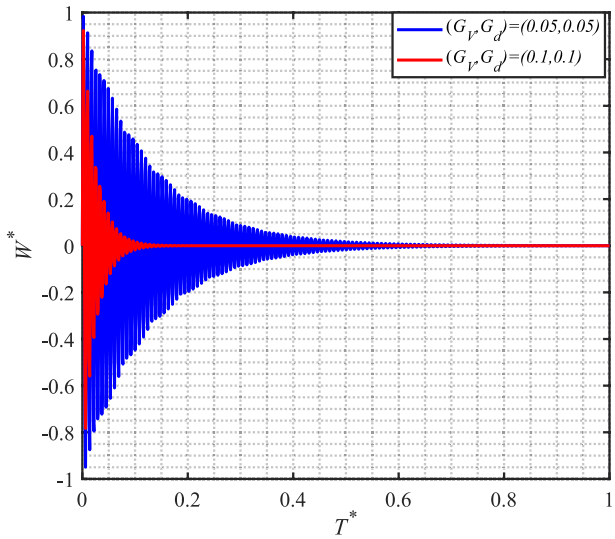

Fig. 6. Vibration response of the controlled system under different sets of PD controller gains. The two curves demonstrate the effect of tuning the dimensionless proportional and derivative gains on the decay rate and stabilization time of the dimensionless deflection.

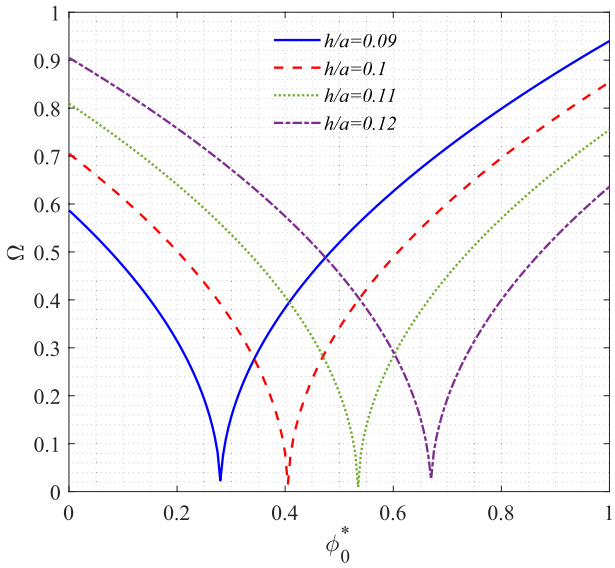

Fig. 7. The dependence of the dimensionless voltage applied on the system's frequency for various height-to-width ratios.

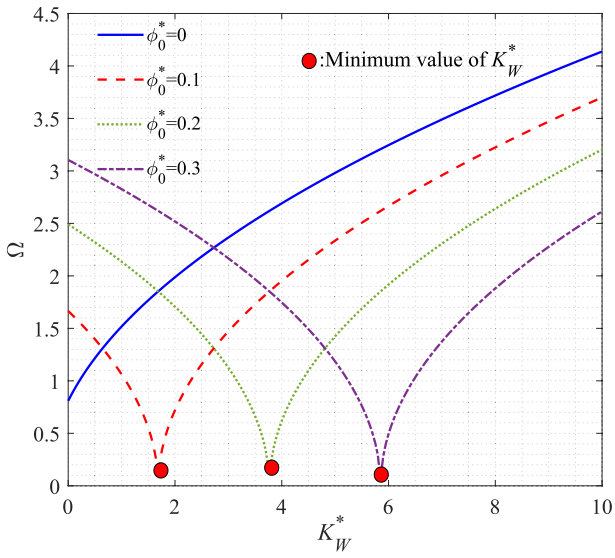

Fig. 8. The dependence of the dimensionless voltage applied on the system's frequency for various dimensionless Winkler coefficients.

Figure 9 illustrates how the frequency of the system and the dimensionless proportional gain coefficient are tied together for various values of applied voltage in a dimensionless way. This control parameter is the one that determines the vibration control system's response time to the changes in dynamic behavior. With the increase in the proportional gain, the system's frequency goes down. Each voltage value is represented with a downward-sloping curve corresponding to the mentioned relationship. The points of the red circles are the minimum points of the proportional gain for each of the applied voltages and are thus the optimal points at which the system's frequency is minimal. The impact of the proportional gain on the system's frequency is more pronounced with higher voltages applied, and hence, it becomes necessary to adjust this parameter for effective vibration control. The importance of such tuning in sports engineering is paramount since there is a demand for real-time adaptability and optimum performance. Just by changing the proportional gain, the system can be made to vibrate less, which, in turn, can greatly improve the performance and longevity of the smart materials that are embedded in sports equipment, thus providing comfort and safety to the users.

In Fig. 10, the correlation between the width-to-height ratio of the plate and the frequency of the system is studied. The ratio has a pronounced effect on the vibrational response of the system, and the plot shows a decrease in frequency with an increase in the ratio. The different levels of applied voltage are depicted with the

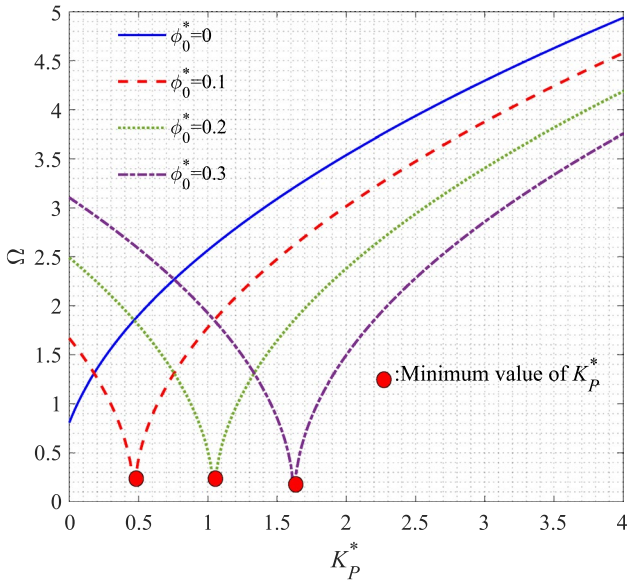

Fig. 9. The dependence of the dimensionless voltage applied on the system's frequency for various dimensionless Pasternak coefficients.

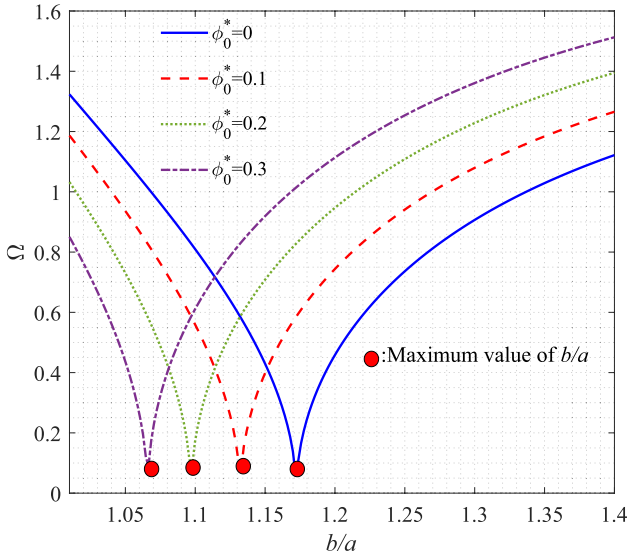

Fig. 10. The dependence of the dimensionless voltage applied on the system's frequency for various b/a parameters.

corresponding curves, which show the influence of voltage on the frequency in relation to the geometric ratio. The red circles marking the curves denote the highest values of the ratio, where the system's frequency has reached its highest value for each voltage condition. Thus, the plot highlights an inverse relation between the width-to-height ratio and frequency. The factor of applied voltage also influences this relation, as higher voltages usually lead to a shift of the system's frequency depending on the geometric configuration of the plate. The findings accentuate the need for changing the width-to-height ratio for frequency control in smart plate systems. In the case of sports engineering applications, where performance optimization is the main objective, this study assists in the design of the plate to achieve very low vibrations, consequently increasing the performance and longevity of the ultra-modern sports equipment.

The relative frequency change (RFC) has been used in this study to illustrate how the frequency depends on the CA-UHPC material. The RFC sensitive to the CA-UHPC material is as follows:

$$RFC_{\mathrm{UHPC}} = |\omega_1 - \omega_2|/\omega_1. \tag{33}$$

The natural frequency of the existing CA-UHPC and epoxy smart structures is shown by ω_1, and ω_2, respectively.

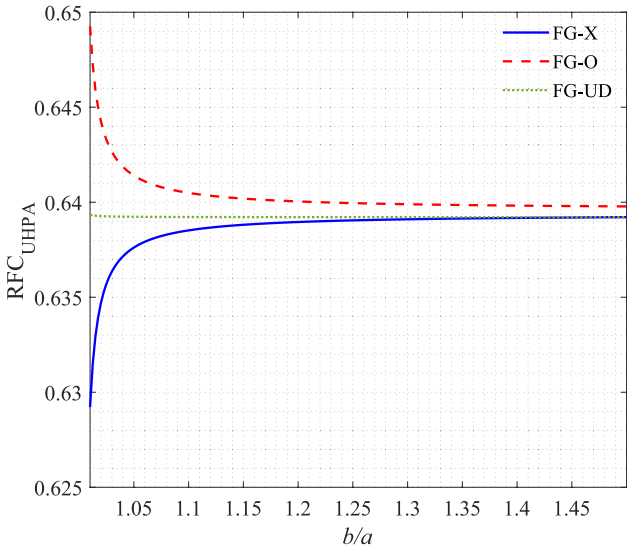

Fig. 11. The relative frequency change of the CA-UHPC smart plate system to illustrate how the frequency depends on the CA-UHPC material for different b/a ratios and CA-UHPC distribution patterns.

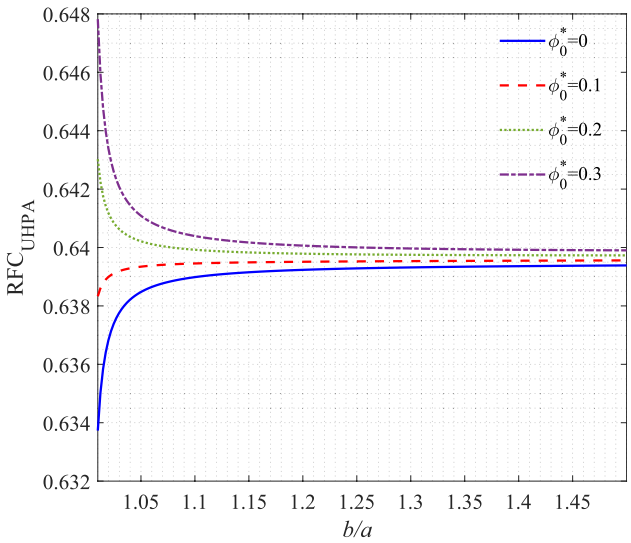

Fig. 12. The relative frequency change of the CA-UHPC smart plate system to illustrate how the frequency depends on the CA-UHPC material for different b/a ratios and dimensionless applied voltages.

$$RFC_{\phi_0} = |\omega_1 - \omega_2|/\omega_1. \tag{34}$$

where ω_1, and ω_2 represent the current smart structure's natural frequency, respectively, with and without taking in-plane voltage into account. Figures 11, 12, 13 and 14 show the sensitivity of the natural frequency of the presented smart structure to the CA-UHPC material. Figure 11 provides evidence of a correlation between the width-to-height ratio of the plate and the relative frequency change of the composite plate to illustrate how the frequency depends on the CA-UHPC material. The three curves represent the different configurations made from the same materials: FG-X, FG-O, and FG-UD. The FG-X configuration is the most favorably positioned relative to frequency change, while FG-O and FG-UD are lower, with FG-UD being the least favorable. There is a trend, however, that is common to all configurations: the frequency change decreases as the width-to-height ratio increases. The figure also conveys that the vibrational characteristics of a plate mainly depend on its geometry and materials' arrangement, especially when the latter vary. This aspect of the relationship is very significant, as it can eventually determine the system's performance in sports engineering, where the right properties of the material and geometry can hugely improve the control of vibrations.

Figure 12 shows how the RFC of the composite plate, at different voltages, is linked to the ratio between the width and the height of the plate. The various voltage curves that are represented are: 0, 0.1, 0.2, and 0.3. The

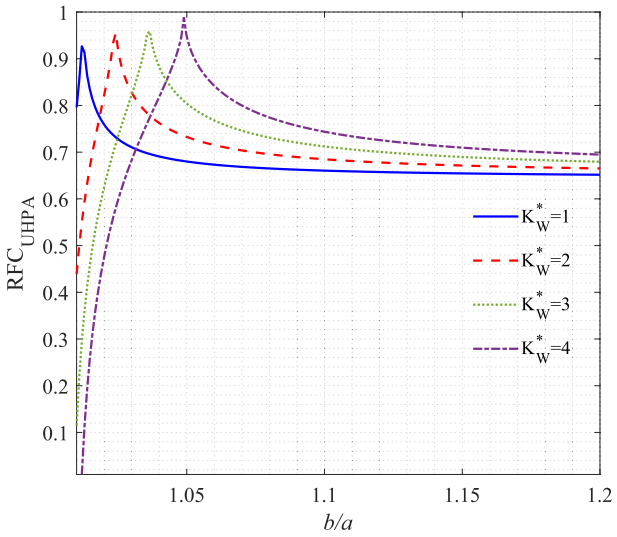

Fig. 13. The relative frequency change of the CA-UHPC smart plate system to illustrate how the frequency depends on the CA-UHPC material for different b/a ratios and dimensionless Winker coefficients.

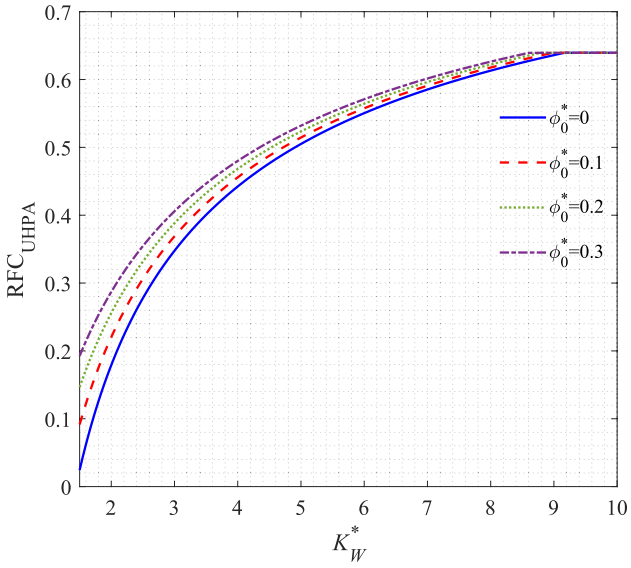

Fig. 14. The relative frequency change of the CA-UHPC smart plate system to illustrate how the frequency depends on the CA-UHPC material for different K_W^* and ϕ_0^* values.

higher the width-to-height ratio, the lower the relative frequency change for all voltage levels. The figure clearly indicates that the change in relative frequency due to the application of voltage is larger, particularly for the low-width-to-height ratios. The voltage effect, however, becomes less significant at the higher ratios since the relative frequency change is almost the same across all voltage levels due to the large ratio. This indicates that the applied voltage, though very important in controlling the dynamic response of the system, will not matter much when adjusting the geometry of the system. This aspect is of great relevance in the case of applications where the voltage conditions adaptability is very momentary, such as in the case of sports engineering, wherein optimizing the material performance could lead to both the durability and multi-functionality of smart plate systems through voltage change control.

For various values of the Winkler coefficient, the correlation between the ratio of the width to the height of the plate and the resultant frequency change of the CA-UHPC smart plate system is illustrated in Fig. 13. The coefficient relates to the interaction between the plate and the foundation. The four curves signify different values of the Winkler coefficient, namely 1, 2, 3, and 4. It is observed that the relative frequency change decreases for all the values of the Winkler coefficient as the width-to-height ratio gets higher. The highest relative frequency change is illustrated, specifically when the width-to-height ratio is small, by the highest Winkler coefficient. This indicates that the higher the stiffness of the foundation, the more the system's vibrational response will be

pronounced and the smaller the geometric ratio. The graph clearly states that the properties of both the material and the foundation should be taken into account when designing systems with the best vibration control. By changing the Winkler coefficient, the system can be accurately tuned to possess the desired vibrational characteristics, which is very much the case in sports engineering, where performance and durability are the main considerations.

Figure 14 reveals the connection between the Winkler coefficient and the RFC of the composite plate for different voltages applied. The figure depicts the influence of the Winkler coefficient variations on the frequency response of the system. The relative frequency change increases with the increase of the Winkler coefficient for all the voltage levels applied. The curves indicate different voltages applied, with the range of the voltage being from 0 to 0.3. The figure indicates that the higher the voltage levels, the greater the relative frequency change across all the Winkler coefficient values. Nevertheless, a considerable Winkler coefficient denotes that the effect of the voltage applied is small, which means that the stiffness of the support has a greater impact on the vibrational behavior of the system. The interaction or coupling here is of great significance for the adjustment or tuning of vibration control in smart plate systems, especially in dynamically changing environments such as sports engineering, where one has to take both material and environmental factors into account to get the best performance.

Figures 15, 16, 17, 18 and 19 show the sensitivity of the natural frequency of the presented smart structure to the in-plane voltage. In Fig. 15, a direct relationship is displayed between the ratio of width to height of the plate and the relative frequency change of the composite plate. Different weight fractions of the material configuration, which are FG-X at 0.1%, 0.2%, 0.3%, and 0.4%, are depicted by the curves. All the ranges of FG-X percentage witness a decline in the relative frequency change as the ratio of width to height increases. This trend reveals that the large plates that possess higher width-to-height ratios are the ones that experience less frequency change. The blue curve, which is related to the material composition of 0.1%, experiences the highest relative frequency change, and this is followed by the red, green, and purple curves, which correspondingly to the material compositions of 0.2%, 0.3%, and 0.4%, register lower relative frequency changes. The current situation brings to the forefront the fact that the selected material significantly impacts the system vibrations. As the plate's shape varies, the graphs fall, demonstrating that even a small fraction of the material determines the stiffness and frequency characteristics of the plate. The whole study is very helpful in the fields of cheap system designing, where material optimization is very much necessary, such as in sports engineering, where both performance and durability are obtained by varying the material's composition and shape.

Figure 16 showcases the correlation between the width-to-height ratio of the plate and the composite plate's relative frequency change for various Winkler foundation coefficients. The curves are for the Winkler coefficient values ranging from 0 to 3. The figure indicates that the relative frequency change decreases with the increase in width to height ratio for all Winkler coefficient values. The Winkler coefficient is a measure of the interaction between the surface and the ground below, so the highest values will be associated with the stiffest foundations. Quite the opposite, the more rigid the foundation, the more pronounced the change in frequency of the system becomes at smaller width-to-height ratios. The frequency change is less at higher ratios, which indicates that the foundation exerts less influence. The investigation reveals that the main influence on vibrating behavior is foundation stiffness; thus, at stiffer foundations, vibration energy has to pass through smaller plate dimensions, and more loss occurs. This interplay is of paramount importance in the design of extremely vibration-sensitive systems, for example, those in high-tech sports engineering, where the foundation's properties are crucial for both performance enhancement and vibration suppression.

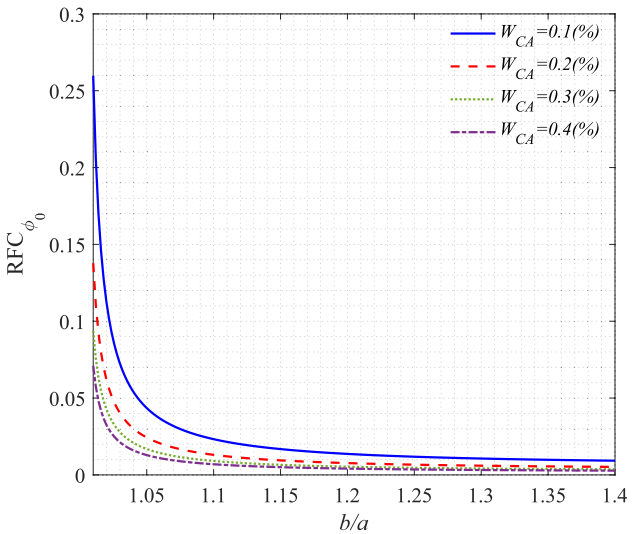

Fig. 15. The relative frequency change of the CA-UHPC smart plate system to illustrate how the frequency depends on the applied voltage for different b/a and W_{CA} values.

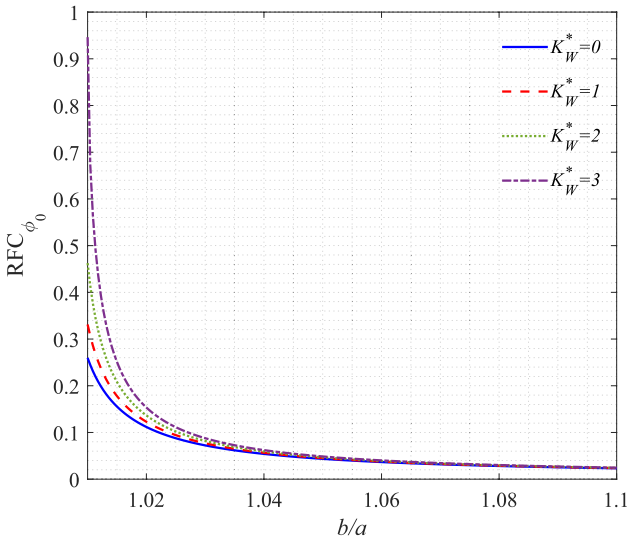

Fig. 16. The relative frequency change of the CA-UHPC smart plate system to illustrate how the frequency depends on the applied voltage for different b/a and K_W^* values.

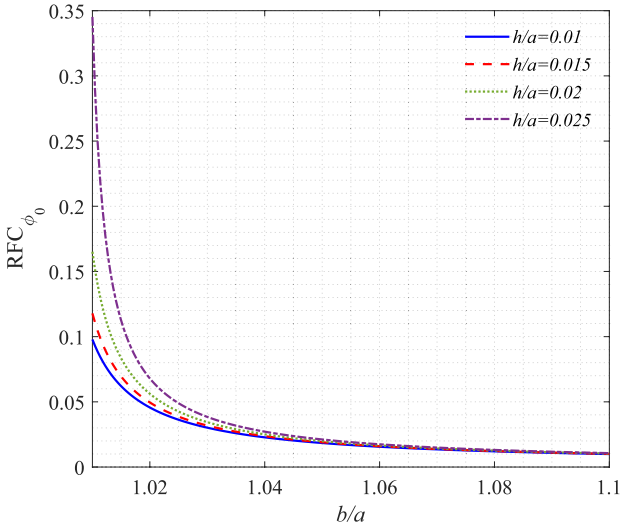

Fig. 17. The relative frequency change of the CA-UHPC smart plate system to illustrate how the frequency depends on the applied voltage for different b/a and h/a values.

In Fig. 17, the height-to-width ratio and the relative frequency change of the composite plate for various ratios are correlated. The different values of the ratio from 0.01 to 0.025 are represented by the curves. The graph reveals that the relative frequency change decreases as the ratio increases, with the decrease being more pronounced for smaller height-to-width ratios. The curves also imply that the smaller plates have the lower height-to-width ratios and thus, the maximum relative frequency changes. This case leads to the conclusion that the geometrical configuration of the plate plays a major role in the vibrational response. It can be added here that the smaller plates are the ones most susceptible to frequency shifts. The curves are gradually lowered as the ratio rises, showing the role of geometry in determining vibrational behavior. This has been precisely recognized as an important factor in scenarios where frequency tuning has to be spot on, for instance, in sports engineering, where one can otherwise easily go wrong with the geometry and get the opposite effects, like performance, environmental noise reduction, and durability improvement, etc.

In Fig. 18, one can see how the Pasternak coefficient interacts with the relative frequency change of the composite plate for the different Pasternak coefficients. The curves reflect the values of the Pasternak coefficient from 0 to 3. The Pasternak coefficient's increment is associated with an equally large relative change in frequency. This suggests that making the foundation stiffer will lead to more pronounced changes in the plate's geometry that will affect the system's vibrational frequency. The plot shows that for plates of less thickness, the change in frequency is mainly determined by the stiffness of the foundation. On the other hand, the bigger the plate,

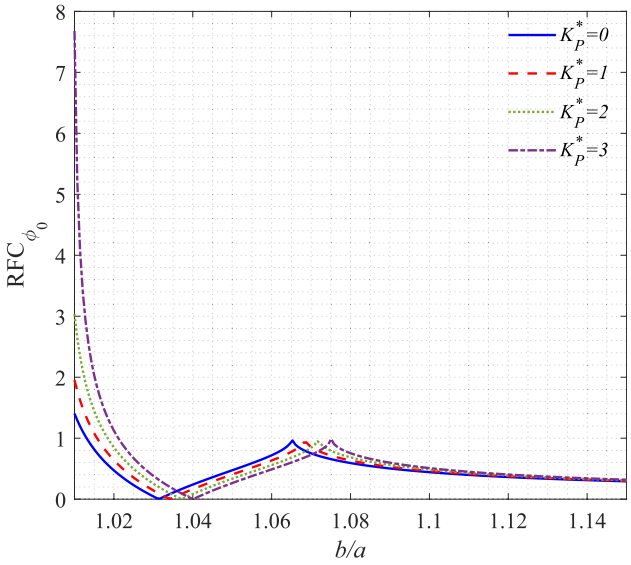

Fig. 18. The relative frequency change of the CA-UHPC smart plate system to illustrate how the frequency depends on the applied voltage for different b/a and K_P^* values.

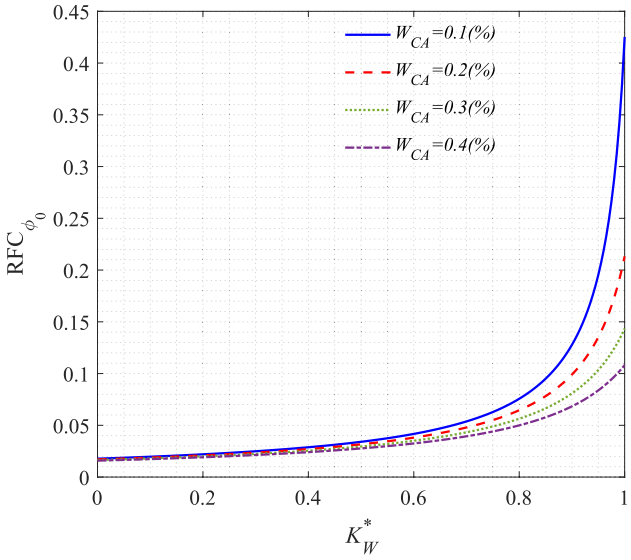

Fig. 19. The relative frequency change of the CA-UHPC smart plate system to illustrate how the frequency depends on the applied voltage for different W_{CA} and K_W^* values.

the less clear the foundation's impact according to the Pasternak coefficient, meaning that for smaller plates, the foundation's influence on the system's frequency is still stronger. This finding points out the role of the foundation's stiffness in vibration control and even more so in case it is necessary to strike a balance between the foundation and plate properties in order to get favorable vibrational characteristics. Such an instance can be seen with top-notch sports gear where the competing factors are stability and performance.

Figure 19 illustrates the association between the dimensionless Winkler coefficient for various material configurations and their corresponding curves. The x-axis represents different percentages of material composition: 0.1%, 0.2%, 0.3%, and 0.4%, with the nomenclature FG-X for the material composition used. On the plot's x-axis, the foundation stiffness is indicated by the dimensionless Winkler coefficient, while the relative frequency change of the CA-UHPC smart plate system is represented on the y-axis. For the increase of the Winkler coefficient, there is a prominent increment in the relative frequency change, and the steepness of the increment becomes greater as the material composition increases. The curve in blue, which stands for 0.1% material, shows the smallest increase in relative frequency, while the other curves, red, green, and purple, which represent 0.2%, 0.3%, and 0.4% material compositions in that order, show the relative frequency increases that are steeper in that order. This phenomenon indicates that the higher the material compositions, the more the vibrational response

Step	Description	Purpose
1. Dataset generation	Execute the PINN framework (Section "PINNs solution procedure") for the defined problem parameters to generate high-fidelity solution fields across the spatio-temporal domain	Creates the reference dataset for supervised learning
2. DNN training	Train a separate, purely data-driven DNN model. Inputs: collocation points. Target outputs: the corresponding PINN-predicted field values	Develops a surrogate model that learns the input–output mapping of the PINN solution
3. Prediction and metric calculation	Use the trained DNN to predict responses for a set of test parameters. Compare U_{DNN} with U_{PINN} using the RMSE and R2 metrics (Eqs. 26, 27)	Quantifies the agreement between the PINN and the verifying DNN model
4. Verification assessment	If RMSE is negligible and $R^2 \approx 1$, the PINN solution is considered consistent and verified by an independent, data-driven approach	Provides an additional layer of confidence in the PINN results' reliability

Table 4. Steps of the DNN-based verification procedure.

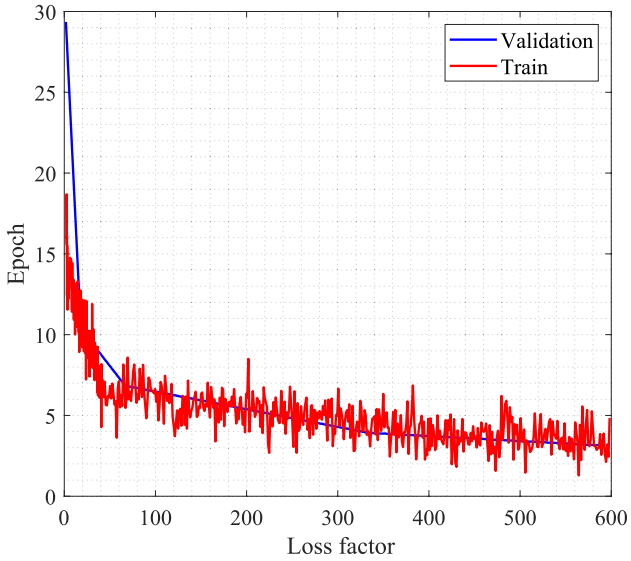

Fig. 20. The training and validation loss values for the DNN algorithm during several epochs.

is affected by the foundation stiffness changes. It is the plot that reveals the mutual dependency between the material properties and the foundation characteristics, indicating that the stiffer foundations produce larger frequency shifts, but in the case of higher material composition, the effect is especially strong. The knowledge of this interaction is very important for the design of systems with the best vibrational control, like in sports engineering, where the relationship between the foundation stiffness and the material composition has to be very precisely calibrated to yield the desired performance.

The outcomes of the DNN method that was described for the given issue

The root mean square error (RMSE) and the coefficient of determination (R2) are the two primary metrics used in this research to assess predictive accuracy. These metrics may be computed using the following methodologies:

$$R^2 = \frac{\sum_{i=1}^{N}(O_i - O_{avg})^2 - \sum_{i=1}^{N}(O_i - y_i)^2}{\sum_{i=1}^{N}(O_i - O_{avg})^2}, \tag{35}$$

$$RMSE = \sqrt{\frac{1}{N}\sum_{i=1}^{N}(O_i - y_i)^2}. \tag{36}$$

The systematic, four-step process for DNN-based verification of the PINN solutions is outlined in Table 4. Initially, the PINN solver is employed to deliver a high-fidelity reference dataset, which is the first step. This dataset is now the basis for training a DNN surrogate model, which is purely data-driven and learns the correspondence between spatio-temporal inputs and the outputs of the PINN model. The next step involves the predictions of the trained DNN being compared with the original result from the PINN using the standard error metrics like root mean square error and the coefficient of determination. The final step is a formal evaluation; the PINN solution is deemed verified if the error is small and R2 is near one. This independent data-driven verification process forms a strong validation of the primary computational method that ensures its reliability and consistency.

Figure 20 reflects the training and validation loss values for the DNN algorithm during several epochs. The x-axis indicates the epoch number, and the y-axis gives the loss factor, which measures the error made by the model during training at every epoch. The red line shows the training loss, which initially has very large

deviations but then more and more steadily drops as the network increments learning from the data. This means the model is getting better and better at its task by adjusting its parameters and reducing error with each iteration. The initial drop followed by sharp fluctuations plot possibly signals the case of overfitting, where the model is becoming increasingly sensitive to the training data, capturing even the noise instead of the pattern. The validation loss that is indicated by the blue curve is usually less volatile than the training loss. Initially, the validation loss falls dramatically, confirming the view that the model is already good at predicting unseen data. After some time, the validation loss becomes constant, implying that the model has reached its maximum limit concerning the capability of generalization. Nevertheless, the difference between the training and validation losses, especially when the former is still sharply fluctuating, indicates that the model might be overfitting the training data. The referred plot serves to provide a vivid depiction of the training process, bringing into the limelight the difficulty of balancing model learning and the risk of overfitting, which is very important for the tuning of the DNN algorithm's performance.

Figure 21 visualizes the comparison of real data versus predicted data through scatter plots for four different cases. Each plot has the true response on the x-axis and the predicted response on the y-axis. The estimated data points are marked by red stars, and a black line confirms the complete correlation between the actual and estimated values. The coefficient of determination (R^2) value, which measures the strength of the relationship between the real and estimated data, is given in each plot. The R^2 value of 0.9998 in the top-left plot indicates that the estimated responses and true ones agree perfectly. The R^2 in the top-right plot is set at 0.9651, revealing

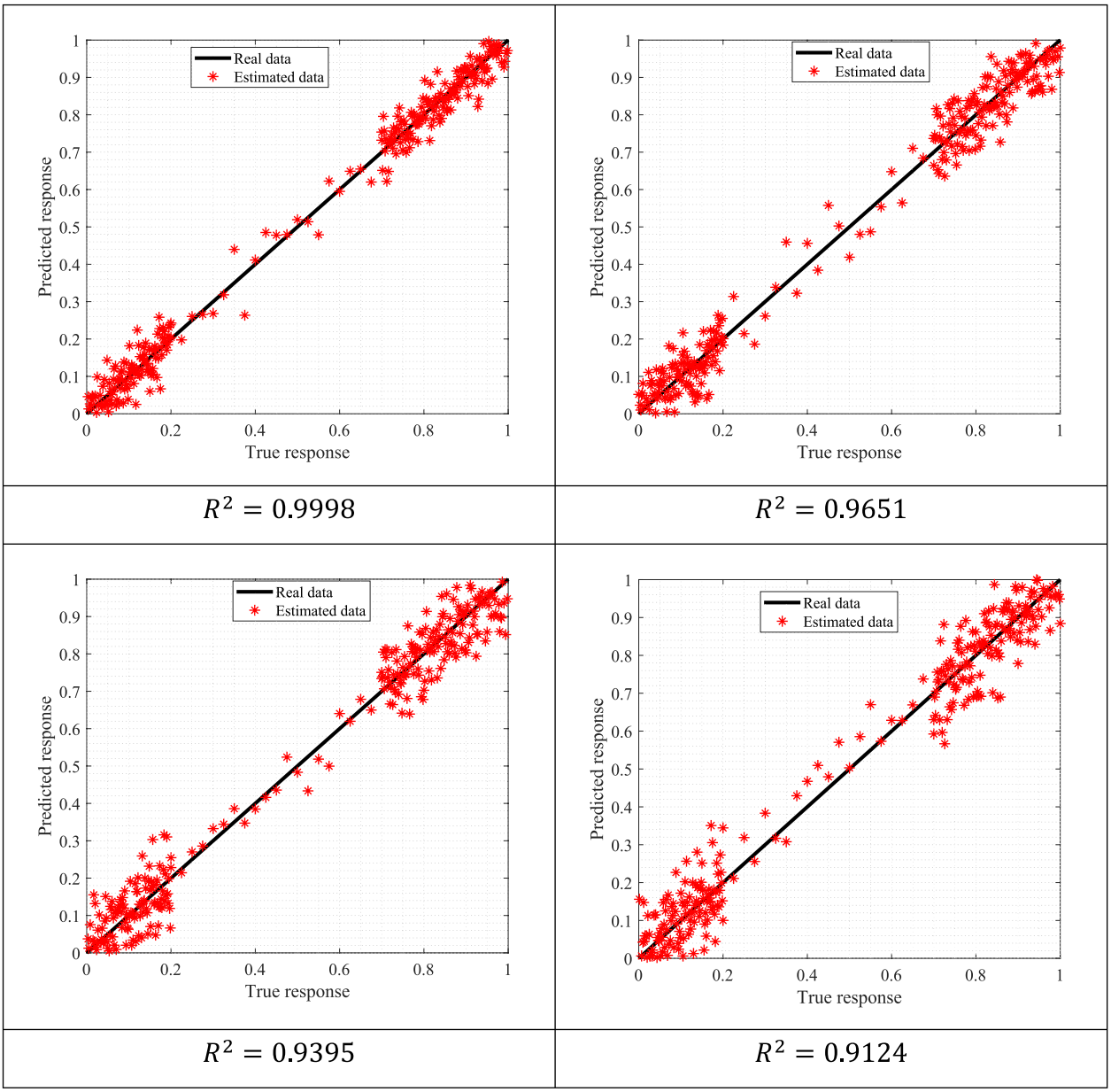

Fig. 21. The comparison of real data versus predicted data through scatter plots for four different cases.

that the correlation is still quite strong but slightly lower than the previous case. The value of R^2 in the bottom-left plot is 0.9395, which means that the predicted and real values have a weak connection but are still considered acceptable. In the bottom-right plot, the R^2 value stands at 0.9124, which, although lower than the previous cases, still signifies a good fit. The plots give insight into how well the predictive model performed and in which cases the estimated responses aligned with the actual ones in the data. The gradual decline in R^2 values indicate that there are some data where the model is not as accurate, but generally, it still works well. It is only natural that noise and complexity, which are common in real-life applications, could have such an impact on the model's precision.

A comprehensive outline of the parameters, along with settings for training of the DNN model created in this research, is in Table 5. The DNN is a five-layer network, with a hidden layer configuration of 128, 64, 32, and 16 neurons, giving about 17,897 trainable parameters. This architecture has been created to provide a compromise between model complexity and computational efficiency. Training configuration: The optimizer that is employed for training is the Adam optimizer, which is an optimization algorithm that is widely accepted due to its efficiency. The initial learning rate is set at 0.001, and the learning rate decay schedule is executed through the Piecewise decay strategy. The LR drop factor is 0.5, and decay occurs every 200 epochs with a maximum of 1000 epochs allowed. The mini-batch size is 8 samples. The activation function used in the hidden layers is the ReLU (Rectified Linear Unit), which is a better choice for convergence in the case of training deep networks. After each hidden layer, batch normalization is applied to stabilize training by reducing internal covariate shift. In data processing, input data is first Z-score normalized, and then output normalization is also done with Z-scores. The train-validation split ratio is 80%-20%, and data shuffling is done. The model has excellent performance, giving an R^2 of 0.9999, which means that the predictions made by the model are very accurate. Besides, the model also has low RMSE, MAE, and MAPE, which indicate that the model makes very small errors, and the model is very reliable.

Table 6 shows the comparison of theoretical results and DNN results for different values of Winkler foundation stiffness and dimensionless applied voltage. In addition, the table provides the absolute error and relative error between the theoretical and DNN results, as well as a verification status for each case. Key Observations: The dimensionless applied voltage is controlled between 0.0 and 0.1, whereas the Winkler foundation stiffness is set from 0.0 to 0.8. These parameters affect the system and are evidenced by both theoretical and DNN results. The absolute error between the theoretical and DNN results is very small throughout the whole simulation, and it ranges from 0.0000 to 0.0002%. This low error range suggests that the DNN model has a high level of accuracy. The relative error remains similarly low, where the maximum error of 0.556% occurs at the configurations with $K_W^* = 0.2$ and $\phi_0^* = 0$, while the minimum relative error of 0.0000% is found with the parameters $K_W^* = 0.2$ and $\phi_0^* = 0.1$. The verification status for every situation is labeled as verified, which means that the DNN results have been compared to the theoretical predictions and the model has been confirmed as trustworthy. All in all, it can

Parameter category	Specific parameter	Value/setting
Network architecture	Number of layers	5 Total layers
	Hidden layer neurons	128–64–32–16
	Total trainable parameters	~17,897
Training configuration	Optimizer	Adam
	Initial learning rate	0.001
	Learning rate schedule	Piecewise decay
	LR drop factor	0.5
	LR drop period	200 epochs
	Maximum epochs	1000
	Mini-batch size	8 Samples
Activation and regularization	Hidden layer activation	ReLU
	Output activation	Linear
	Batch normalization	After each hidden layer
	L1/L2 regularization	None applied
Data processing	Input normalization	Z-score ($\mu = 0, \sigma = 1$)
	Output normalization	Z-score ($\mu = 0, \sigma = 1$)
	Train-validation split	80–20%
	Data shuffling	Every epoch
Performance results	R^2 (Coefficient of determination)	0.999998
	RMSE (Root mean square error)	0.000215
	MAE (Mean absolute error)	0.000142
	MAPE (Mean absolute percentage error)	0.0008%

Table 5. A comprehensive outline of the parameters, along with settings for training of the DNN model created in this research.

K_W^*	ϕ_0^*	Theoretical results	DNN results	Absolute error	Relative error	Verification status
0.0	0.0	0.600	0.6002	0.0002	0.033	✓ Verified
0.0	0.1	0.500	0.4998	0.0002	0.040	✓ Verified
0.2	0.0	0.018	0.0181	0.0001	0.556	✓ Verified
0.2	0.1	0.019	0.0190	0.0000	0.000	✓ Verified
0.4	0.0	0.022	0.0221	0.0001	0.455	✓ Verified
0.4	0.1	0.023	0.0229	0.0001	0.435	✓ Verified
0.6	0.0	0.028	0.0281	0.0001	0.357	✓ Verified
0.6	0.1	0.030	0.0299	0.0001	0.333	✓ Verified
0.8	0.0	0.045	0.0451	0.0001	0.222	✓ Verified
0.8	0.1	0.050	0.0499	0.0001	0.200	✓ Verified

Table 6. The RFC comparison of theoretical results and DNN results for different values of Winkler foundation stiffness and dimensionless applied voltage.

be inferred from the table that the DNN model generates results that are in close proximity to the theoretical predictions, with practically no errors, and also has successful verification for the entire set of cases tested.

Conclusion

In this work, an innovative vibration control technique based on AI and connected systems was proposed, designed with advanced composite materials and intelligent algorithms. In the end, the study has exhibited a sustainable and efficient method of vibration suppression, especially for the next-generation sports engineering, by embedding the piezoelectric face sheets in a coarse aggregate ultra-high-performance concrete core. The combination of the Halpin–Tsai models and the law of mixtures has made it possible to accurately predict the material properties, which is a key factor for the performance of the material under dynamic loading conditions. The quasi-3D theory of four variables has greatly contributed to the comprehension of transversal shear strains and stresses throughout the plate thickness, thus providing a more realistic characterization of structural behavior. The forecasts of the system's dynamic responses were able to reach a higher level of precision, mainly for those subjected to complicated boundary conditions. The use of piezoelasticity theory and the Hamilton principle has not only laid a solid foundation for the determination of the governing equations that characterize the vibration performance under various loading conditions, but also allowed the distribution of elastic foundation represented by both Winkler and Pasternak coefficients to add more realism to the interactions between the plate and the support. This turning point played an important role in the creation of a more accurate model for the real world, which typically has non-ideal boundary conditions. Traditional Legendre polynomial expansions have been replaced by the PINN, leading to a more efficient solution process. This AI-assisted technique is twofold: it has not only boosted the computational performance but also made it possible to carry out dynamic condition-adaptive real-time control adjustments. A DNN-based verification procedure has been employed to corroborate the results of this research, thereby affirming the reliability and precision of the suggested method for vibration control. The progression made has taken the traditional vibration control method in smart sports engineering to a whole new level, making it possible to continuously improve sports equipment of the next generation in a sustainable and non-wasteful manner.

Data availability

The datasets used and/or analysed during the current study are available from the corresponding author on reasonable request.

Received: 22 December 2025; Accepted: 20 February 2026
Published online: 02 April 2026

References

1. Dadashi, P., Torbatinejad, K. & Babaei, A. Hybridization as a promising approach to engineering the desired performance of bio-nanocomposites: GO-ZnO hybrid reinforced PCL. *Sci. Rep.* **15**, 17259 (2025).
2. Wang, P., Liu, B. Q., Peng, X. T. & Gao, F. Bending and vibration behavior of functionally graded piezoelectric nanobeams considering dynamic flexoelectric and surface effects. *Sci. Rep.* **15**, 13439 (2025).
3. Zhang, P., Wang, Z., Tian, H., Xi, X. & Liu, X. On the magnetically tunable free damped-vibration of L-shaped composite spherical panels made of GPL-reinforced magnetorheological elastomers: an element-based GDQ approach. *Thin-Walled Struct.* **218**, 113987 (2025).
4. Akbari, M., Sadighi, M., Eslami, M. & Kiani, Y. Axisymmetric free vibration analysis of functionally graded sandwich annular plates: A Quasi-3D shear and normal deformable model. *Int. J. Struct. Stab. Dyn.* **23**, 2350086 (2023).
5. Mei, J., Wu, Z. & Kou, J. Moving-load dynamic analysis of graphene-reinforced metal foam arches covered with titanium alloy layers. *Int. J. Str. Stab. Dyn.* https://doi.org/10.1142/S0219455426501737 (2025).
6. Zhang, Y. & Peng, J. In-plane vibrations of deep sandwich arches with different end conditions based on a logarithmic shear deformation theory. *Int. J. Str. Stab. Dyn.* **25**, 2550029. https://doi.org/10.1142/S0219455425500294 (2025).
7. Lu, S. F., Xue, N., Ma, W. S., Song, X. J. & Jiang, X. Linear and nonlinear dynamics responses of an axially moving laminated composite plate-reinforced with graphene nanoplatelets. *Int. J. Str. Stab. Dyn.* **25**, 2550036. https://doi.org/10.1142/S0219455425500361 (2025).

8. Peng, S., Gao, J. & Wu, Z. Thermal and mechanical bifurcation stability analyses of clamped hybrid dual-FG composite annular and circular plates. *Int. J. Str. Stab. Dyn.* https://doi.org/10.1142/S0219455426501087 (2024).
9. Wang, X. Application of electrorheological fluid cores to improve the vibration response of sandwich toroidal shell elements covered by functionally graded nanocomposite faces. *Int. J. Str. Stab. Dyn.* https://doi.org/10.1142/S0219455426501488 (2025).
10. Raju, G. H. T., Vembu, V., Raju, P. R., Ganesan, G. & Narendar, S. Influences of external magnetic field on thermo-mechanical vibration analysis of nanocomposite beam using higher-order strain gradient theory. *Int. J. Str. Stab. Dyn.* **25**, 2440008. https://doi.org/10.1142/S021945542440008X (2025).
11. Du, G. et al. Study on automatic tracking system of microwave deicing device for railway contact wire. *IEEE Trans. Instrum. Meas.* **73**, 1–11 (2024).
12. Xu, X. & Li, B. PDE-based observation and predictor-based control for linear systems with distributed infinite input and output delays. *Automatica* **170**, 111845 (2024).
13. Zhao, D. & Zeng, S. Recurrent neural network solver for structural motion differential equations. Int. J. Struct. Stab. Dyn. (2024).
14. Yin, Q., Xin, T., Zhenggang, H. & Minghua, H. Measurement and analysis of deformation of underlying tunnel induced by foundation pit excavation. *Adv. Civ. Eng.* **2023**, 8897139 (2023).
15. Tang, C. et al. Coupled vibratory roller and layered unsaturated subgrade model for intelligent compaction. *Comput. Geotech.* **177**, 106827 (2025).
16. Deng, J. & Gao, N. Broadband vibroacoustic reduction for a circular beam coupled with a curved acoustic black hole via nullspace method. *Int. J. Mech. Sci.* **233**, 107641 (2022).
17. Deng, J. et al. Vibration damping by periodic additive acoustic black holes. *J. Sound Vib.* **574**, 118235 (2024).
18. Zhang, W., Zhang, B., Jin, S., Shen, H. & Li, C. Size-dependent dynamics of rotating FG imperfect microplates under in-plane loads using an improved differential quadrature finite element method. *Thin-Walled Struct.* **212**, 113204 (2025).
19. Xiong, J. & Chen, Y. RBFNN-based parameter adaptive sliding mode control for an uncertain TQUAV with time-varying mass. *Int. J. Robust Nonlinear Control* **35**, 4658–4668 (2025).
20. Hu, D. et al. Calculation methods for the jacking force of a rectangular pipe jacking tunnel: Overview and prospects. *J. Pipeline Syst. Eng. Pract.* **16**, 03125001 (2025).
21. Wang, H., Wu, S., Yu, F., Bi, Y. & Xu, Z. Study on remaining useful life prediction of sliding bearings in nuclear power plant shielded pumps based on nearest similar distance particle filtering. *Ann. Nucl. Energy* **223**, 111625 (2025).
22. W. Cui, L. Zhao, Y. Ge, K. Xu, A generalized van der Pol nonlinear model of vortex-induced vibrations of bridge decks with multistability. *Nonlinear Dyn.* 1–14 (2023).
23. Yang, J., Liu, Y., Lu, X. & Wang, T. An adaptive measurement-based substructure identification framework for dynamic response reconstruction. Available at SSRN 5186270 (n.d.).
24. Dai, J. et al. Robust damping improvement against the vortex-induced vibration in flexible bridges using multiple tuned mass damper inerters. *Eng. Struct.* **313**, 118221 (2024).
25. Gai, P.-P., Dai, J., Xu, Z.-D., Bi, Q.-S. & Guan, Q.-S. A novel two-state active tuned mass damper inerter control of high-flexibility long-span bridges. *J. Struct. Eng.* **151**, 05025005 (2025).
26. Hao, R.-B., Lu, Z.-Q., Ding, H. & Chen, L.-Q. A nonlinear vibration isolator supported on a flexible plate: Analysis and experiment. *Nonlinear Dyn.* **108**, 941–958 (2022).
27. Lu, Z., Brennan, M. J., Yang, T., Li, X. & Liu, Z. An investigation of a two-stage nonlinear vibration isolation system. *J. Sound Vib.* **332**, 1456–1464 (2013).
28. Ren, K. et al. Probing to dynamics of a tube-core sandwich enhanced liquid-filled tank subjected to hydrodynamic ram. *Thin-Walled Struct* **215**, 113573 (2025).
29. Yang, X., Puig, V., Wang, X., Wang, S., Sun, C. & Zhang, Y. Dynamic-high-gain-based decentralized optimal fault-tolerant control for a class of interconnected nonlinear systems. *IEEE Trans. Autom. Control* (2025).
30. Avcar, M., Hadji, L. & Civalek, O. The influence of non-linear carbon nanotube reinforcement on the natural frequencies of composite beams. *Adv. Nano Res.* **14**, 421–433 (2023).
31. Zhu, Z., Liu, Y., Gou, G., Gao, W. & Chen, J. Effect of heat input on interfacial characterization of the butter joint of hot-rolling CP-Ti/Q235 bimetallic sheets by Laser+ CMT. *Sci. Rep.* **11**, 10020 (2021).
32. Zhang, Y., Xu, Y., Zhou, J., Zhou, Y. & Mahfoud, J. Vibration control of AMB-rotor system under base motions based on disturbance observer. *IEEE/ASME Trans. Mechatron.* (2025).
33. He, D. et al. Nonlinear vibration and vibration transmission of roll controlled by negative stiffness vibration absorbers. *Mech. Syst. Signal Process.* **245**, 113872 (2026).
34. Hu, D. et al. Machine learning–finite element mesh optimization-based modeling and prediction of excavation-induced shield tunnel ground settlement. *Int. J. Comput. Methods* **22**, 2450066 (2024).
35. Wang, H., Li, Y.-F., Men, T. & Li, L. Physically interpretable wavelet-guided networks with dynamic frequency decomposition for machine intelligence fault prediction. *IEEE Trans. Syst. Man Cybern. Syst.* **54**, 4863–4875 (2024).
36. Li, Y., Weng, X., Hu, D., Tan, Z. & Liu, J. Data-driven method for predicting long-term underground pipeline settlement induced by rectangular pipe jacking tunnel construction. *J. Pipeline Syst. Eng. Pract.* **16**, 04025046 (2025).
37. Wang, Q., Cao, J. & Liu, H. Adaptive fuzzy control of nonlinear systems with predefined time and accuracy. *IEEE Trans. Fuzzy Syst.* **30**, 5152–5165 (2022).
38. He, L. et al. Machine-learning-driven on-demand design of phononic beams. *Sci. China Phys. Mech. Astron.* **65**, 214612 (2022).
39. Hu, X. et al. Pcastnet: A physics-constrained adaptive style transfer network for sample generation in cross-machine small-sample fault diagnosis. *IEEE Trans. Instrum. Meas.* **74**, 1–17 (2025).
40. Wan, A. et al. Vibration prediction for abnormal elevator door system faults based on attention mechanism and neural networks with time-frequency domain features. *Proc. Inst. Mech. Eng. C. J. Mech. Eng. Sci.* **239**, 7358–7372 (2025).
41. Yan, C., Vescovini, R. & Dozio, L. A framework based on physics-informed neural networks and extreme learning for the analysis of composite structures. *Comput. Struct.* **265**, 106761 (2022).
42. Yang, H. et al. The global industrial robot trade network: Evolution and China's rising international competitiveness. *Systems* **13**, 361 (2025).
43. Nguyen, N.-T., Hui, D., Lee, J. & Nguyen-Xuan, H. An efficient computational approach for size-dependent analysis of functionally graded nanoplates. *Comput. Methods Appl. Mech. Eng.* **297**, 191–218 (2015).
44. Reddy, J. N. *Mechanics of laminated composite plates and shells: theory and analysis* (CRC Press, Boca Raton, 2003).
45. Tandis, N. & Tandis, E. A physics-informed machine learning approach to piezoelectric plate modelling. *Eng. Appl. Artif. Intell.* **160**, 111847 (2025).
46. Mirzaei, M. Vibration characteristics of sandwich plates with GPLRC core and piezoelectric face sheets with various electrical and mechanical boundary conditions. *Mech. Based Des. Struct. Mach.* **52**, 990–1013 (2024).
47. Baferani, A. H., Saidi, A. & Ehteshami, H. Accurate solution for free vibration analysis of functionally graded thick rectangular plates resting on elastic foundation. *Compos. Struct.* **93**, 1842–1853 (2011).
48. Cain, M. G. & Stewart, M. Standards for piezoelectric and ferroelectric ceramics. In: *Characterisation of Ferroelectric Bulk Materials and Thin Films* 267–275 (Springer, 2014).

Acknowledgements
This work was supported by the Science and Technology Research Program of Chongqing Municipal Education Commission (Grant No. KJQN202502909); And the Chongqing Preschool Education College Scientific Research Platform in 2024 (Grant Number: 2024KYPT-01).

Author contributions
Bing Lin: Conceptualization, Investigation, Methodology, Reviewing and Editing, Solution Approach. Jinyu Wang: Conceptualization, Investigation, Methodology, Reviewing and Editing. Mehran Safarpour: Software, Supervision, Writing-Original draft preparation, Reviewing and Editing. Murat Yaylacı: Software, Reviewing and Editing, Writing-Original draft preparation.

Funding
There was no Funding.

Competing interests
The authors declare no competing interests.

Additional information
Correspondence and requests for materials should be addressed to M.S.

Reprints and permissions information is available at www.nature.com/reprints.

Publisher's note Springer Nature remains neutral with regard to jurisdictional claims in published maps and institutional affiliations.